The University of Sydney

School of Civil Engineering
Sydney NSW 2006
AUSTRALIA

http://www.civil.usyd.edu.au/

Centre for Advanced Structural Engineering

Geometric Nonlinear Isoparametric Spline Finite Strip Analysis of Perforated Thin-Walled Structures

Research Report No R880

Gabriele Eccher MEng
Kim J. R. Rasmussen MScEng PhD
Riccardo Zandonini MEng PhD

February 2007

The University of Sydney

School of Civil Engineering
Centre for Advanced Structural Engineering
http://www.civil.usyd.edu.au/

Geometric Nonlinear Isoparametric Spline Finite Strip Analysis of Perforated Thin-Walled Structures

Research Report No R880

Gabriele Eccher MEng
Kim J. R. Rasmussen MScEng PhD
Riccardo Zandonini MEng PhD

February 2007

Abstract:
In previous reports [1, 2], the isoparametric spline finite strip method was successfully applied to the in-plane stress and bending linear elastic analysis of perforated plates. The method has been successfully applied to the elastic linear analysis and buckling analysis of folded plate structures [3, 4]. In the present report the application of the isoparametric spline finite strip method is further extended to the geometric nonlinear analysis of perforated folded plate structures.

The general theory of the isoparametric spline finite strip method is briefly introduced. Kinematics, strain-displacements and constitutive assumptions are described and applied to the spline finite strip method. The derivation of the tangential and secant stiffness matrices is presented by applying the equilibrium condition and its incremental form. A large part of report is reserved to a review of the available nonlinear solution techniques, notably the cylindrical arc-length method. Classical nonlinear complex plate and shell problems are analysed and compared with exact solutions or with well established numerical results in order to demonstrate the reliability of the method. Furthermore, examples of the geometric nonlinear analysis of perforated flat and stiffened plates are included to highlight the effect of perforations on the behaviour of thin plate elements.

Keywords:
Folded plate structures, geometric nonlinear analysis, isoparametric spline finite strip method, perforations, thin-walled elements, local buckling, distortional buckling.

Copyright Notice

School of Civil Engineering, Research Report R880
Geometric Nonlinear Isoparametric Spline Finite Strip Analysis of Perforated Thin-Walled Structures

G.Eccher@civil.usyd.edu.au, K.Rasmussen@civil.usyd.edu.au and Riccardo.Zandonini@ing.unitn.it

Published by:
School of Civil Engineering
The University of Sydney
Sydney NSW 2006
AUSTRALIA

February 2007

This report and other Research Reports published by The School of Civil Engineering are available on the Internet:

http://www.civil.usyd.edu.au

TABLE OF CONTENTS

Introduction

The Spline Finite Strip Method was developed from the semi-analytical Finite Strip Method originally derived by Cheung [5]. The Finite Strip Method was based on harmonic functions, and proved to be an efficient tool for analysing structures with constant geometrical properties along a particular direction, generally the longitudinal one. The spline finite strip method complemented the semi-analytical finite strip method by allowing more complex types of loading and support conditions to be modelled at the expense of a more comprehensive set of displacement functions based on splines. Initially introduced for the static linear and free vibration analyses of flat plates [6], the spline finite strip method was fully developed for the linear elastic structural analysis of folded plate structures by Fan and Cheung [7]. The spline finite strip method was then extended to the buckling and nonlinear analyses of flat plates and folded-plate structures by Hancock and co-workers [8-10]. Subsequently, the isoparametric concept was applied to the spline finite strip method by Au and Cheung for the linear in-plane stress and bending analyses of Mindlin plates [11] and degenerated shells [12]. This extension allowed structures having a distorted longitudinal axis to be efficiently analysed with the finite strip method.

The present work originates from the industrial and civil applications of thin-walled structural members with perforations, which can be modelled as complex systems of thin plates. Holes and cut-outs of various shapes are used in practice to ease the assembly of structures [13], or to allow the passage of services, but introduce discontinuities in the cross-section and, consequently, a redistribution of the membrane stresses within the members. Extensive research has been undertaken in the last two decades studying the behaviour of thin plates containing cut-outs of different shapes [14], beams with holes in the web [15] and industrial rack uprights with closely spaced cut-outs [16], highlighting the complexity of the analysis of such structures. The shape of the hole, its position within the cross-section, its dimensions and its longitudinal spacing [17] are the most important parameters defining the global behaviour of the member but it is difficult to combine these factors into simple design guidelines for predicting the ultimate strength. Existing design rules are therefore empirical and only valid in the parameter ranges investigated.

Within this general framework, the authors aim to develop an efficient numerical tool that applies the efficiency of the isoparametric spline finite strip method to the complex analysis of perforated thin-walled structures. The method has been successfully applied by the authors to the linear elastic and buckling analyses of perforated plates and prismatic perforated folded plate structures [1-4]. The present report extends the application of the isoparametric spline finite strip method to the geometrical nonlinear analysis.

The displacement functions, strain-displacement relations and constitutive material model used for the elastic nonlinear theory are described. Subsequently, the nonlinear equilibrium equation and its incremental form are set out. The relevant strain and constitutive matrices are derived, as are the

tangential and secant stiffness matrices obtained by applying the equilibrium condition and its incremental form.

The numerical technique utilised for solving the nonlinear equations is presented and commented on in detail. A review of existing solution techniques is given with particular focus on the cylindrical arc-length method.

The reliability of the geometric nonlinear isoparametric spline finite strip analysis is demonstrated by comparisons with finely meshed finite element analyses. Classical nonlinear complex plate and shell problems are analysed and compared with exact solutions or with well established numerical results in order to demonstrate the reliability of the solution technique utilised. Furthermore, examples of the geometric nonlinear analysis of perforated flat and stiffened plates are included.

Isoparametric Spline Finite Strip Method

A finite strip is a particular type of finite element, geometrically characterized by having one dimension, the longitudinal one, much greater than the transverse one. The shape functions defined over a plane finite strip differ from those of the plane finite element because the former are expressed in terms of a combination of two families of functions, one depending on the transverse coordinate and one on the longitudinal coordinate. For a bi-dimensional finite strip, the transverse shape functions generally correspond to the finite element shape functions utilized in one-dimensional elements, while trigonometric, exponential or spline series may be utilized for the longitudinal shape functions. Within a finite strip, the nodes are distributed along longitudinal paths called nodal lines. The number of nodes along each nodal line depends on the number of the longitudinal series components, while the number of nodal lines defining a strip is determined by the order of the transverse shape functions, i.e. two nodal lines for linear shape functions, three for quadratic, four for cubic and so on.

In the present work, Lagrangian cubic transverse shape functions and cubic B_3-Spline longitudinal series functions have been utilized.

The transverse cubic shape functions are given by

$$L_1(\xi) = -\frac{9}{16}\left(\xi^3 - \xi^2 - \frac{1}{9}\xi + \frac{1}{9}\right) \tag{1}$$

$$L_2(\xi) = \frac{27}{16}\left(\xi^3 - \frac{1}{3}\xi^2 - \xi + \frac{1}{3}\right) \tag{2}$$

$$L_3(\xi) = -\frac{27}{16}\left(\xi^3 + \frac{1}{3}\xi^2 - \xi - \frac{1}{3}\right) \tag{3}$$

$$L_4(\xi) = \frac{9}{16}\left(\xi^3 + \xi^2 - \frac{1}{9}\xi - \frac{1}{9}\right) \tag{4}$$

where $L_i(\xi)$ is the component of the shape functions referring to the i^{th} nodal line of the strip and ξ is the transverse curvilinear coordinate. A graphic representation of the transverse shape functions is given in Fig. 1. It follows that the finite strip utilized in the present work is defined by a set of four nodal lines.

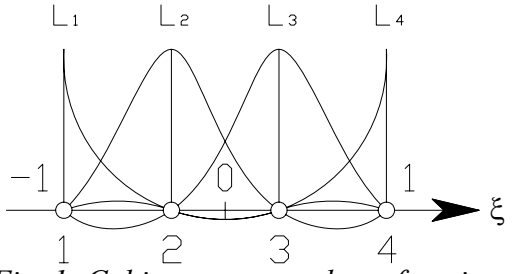

Fig. 1: Cubic transverse shape functions.

The general component of the B_3-Spline series is expressed by

$$\phi_j(\eta)=\frac{1}{6}\begin{cases}0 & ,\ \eta<\eta_{j-2}\\ \left(\eta-\eta_{j-2}\right)^3 & ,\ \eta_{j-2}\le\eta<\eta_{j-1}\\ 1+3\left(\eta-\eta_{j-1}\right)+3\left(\eta-\eta_{j-1}\right)^2-3\left(\eta-\eta_{j-1}\right)^3 & ,\ \eta_{j-1}\le\eta<\eta_j\\ 1+3\left(\eta_{j+1}-\eta\right)+3\left(\eta_{j+1}-\eta\right)^2-3\left(\eta_{j+1}-\eta\right)^3 & ,\ \eta_j\le\eta<\eta_{j+1}\\ \left(\eta_{j+2}-\eta\right)^3 & ,\ \eta_{j+1}\le\eta<\eta_{j+2}\\ 0 & ,\ \eta>\eta_{j+2}\end{cases} \tag{5}$$

where $\phi_j(\eta)$ represents the j^{th} component of the cubic spline series and η is the longitudinal curvilinear coordinate. Its shape is shown in Fig. 2 (a). In (5), the indexed longitudinal curvilinear coordinates, η_j, are the coordinates of the nodes which are spaced by a unit distance. By inspection of (5) and Fig. 2 (a), it follows that the generic j^{th} spline component is defined over four consecutive sections and centered on the j^{th} node. A full B_3-Spline series comprises m+3 components, i.e. m+3 nodes per nodal line, as shown in Fig. 2 (b), where with "m" we denote the number of sections subdividing the strip and, consequently, each nodal line. It also follows that the coordinate η spans from zero to m between the two ends.

The general displacement function defined within a strip of uniform thickness, t, can be expressed in terms of the curvilinear coordinate system by the B_3-spline and Lagrangian shape functions as follows

$$\delta(\xi,\eta)=\sum_{i=1}^{4}\sum_{j=-1}^{m+1}L_i(\xi)\,\phi_j(\eta)\,\alpha_{ij}^{\delta} \tag{6}$$

where δ represents the generic generalized displacement function and the numerical coefficient α_{ij}^{δ} represents the generalized variable which refers to the displacement function δ on the i^{th} nodal line and at the j^{th} node.

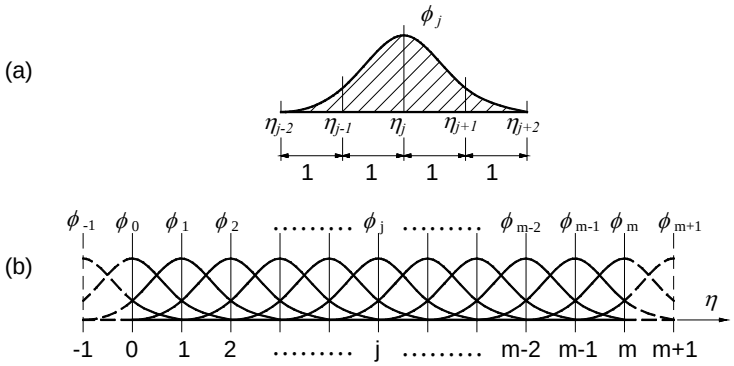

Fig. 2: (a) - j-th component of the B_3-Spline; (b) – a complete B_3-Spline series.

Introducing now the shape function N_{ij} as

$$N_{ij}(\xi,\eta) = L_i(\xi)\,\phi_j(\eta) \tag{7}$$

a compact formulation of the general displacement function is given by

$$\delta(\xi,\eta) = \sum_{i=1}^{4}\sum_{j=-1}^{m+1} N_{ij}(\xi,\eta)\,\alpha_{ij}^{\delta} \tag{8}$$

It is convenient to introduce a matrix formulation for the general displacement field δ as follows

$$\delta = \mathbf{N}\,\boldsymbol{\alpha} \tag{9}$$

where

$$\mathbf{N} = \begin{bmatrix}\mathbf{N}_1 & \mathbf{N}_2 & \mathbf{N}_3 & \mathbf{N}_4\end{bmatrix} \tag{10}$$

$$\boldsymbol{\alpha} = \begin{bmatrix}\boldsymbol{\alpha}_1^{\delta T} & \boldsymbol{\alpha}_2^{\delta T} & \boldsymbol{\alpha}_3^{\delta T} & \boldsymbol{\alpha}_4^{\delta T}\end{bmatrix}^T \tag{11}$$

In (10) and (11) the generic sub-matrix $\mathbf{N}_i$ and the sub-vector $\boldsymbol{\alpha}_i^{\delta}$ are given by

$$\mathbf{N}_i = L_i(\xi)\begin{bmatrix}\phi_{-1}(\eta) & \phi_0(\eta) & \phi_1(\eta) & \cdots & \phi_m(\eta) & \phi_{m+1}(\eta)\end{bmatrix} \tag{12}$$

$$\boldsymbol{\alpha}_i^{\delta} = \begin{bmatrix}\alpha_{i\,-1}^{\delta} & \alpha_{i\,0}^{\delta} & \alpha_{i\,1}^{\delta} & \cdots & \alpha_{i\,m}^{\delta} & \alpha_{i\,m+1}^{\delta}\end{bmatrix}^T \tag{13}$$

Mapping

A generic cubic isoparametric spline finite strip is illustrated in Fig. 3. Fig. 3(a) shows its representation in the local Cartesian coordinate system while Fig. 3(b) shows its mapping into the curvilinear coordinate system.

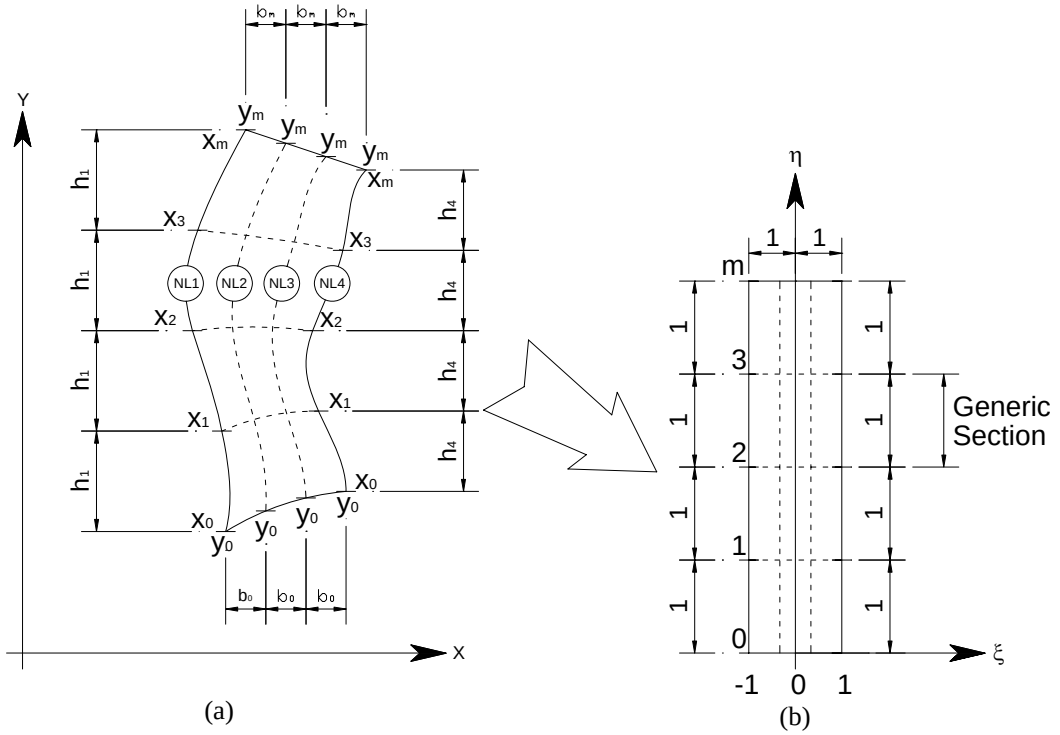

Fig. 3: (a) Generic cubic strip in the local Cartesian coordinate system; (b) Generic strip mapped into the curvilinear coordinate system

Dealing with plane strips, the position of the generic point of the mid-surface is simply defined by the Cartesian coordinates x and y. They are expressed in terms of the curvilinear coordinates ξ and η by

$$x(\xi,\eta)=\sum_{i=1}^{4}\sum_{j=-1}^{m+1}L_i(\xi)\phi_j(\eta)\overline{\beta}_{ij}^{x} \tag{14}$$

$$y(\xi,\eta)=\sum_{i=1}^{4}\sum_{j=-1}^{m+1}L_i(\xi)\phi_j(\eta)\overline{\beta}_{ij}^{y} \tag{15}$$

where $\overline{\beta}_{ij}^{x}$ and $\overline{\beta}_{ij}^{y}$ are numerical coefficients to be determined from the geometry. They comprise 4(m+3) coefficients for each coordinate.

As shown in [1], the number of geometrical coefficients can be reduced to those lying on the perimeter of the strip by using an appropriate pre-determined choice of the location of the internal nodes. (14) and (15) can be rewritten as

$$x(\xi,\eta)=\sum_{j=-1}^{m_s+1}\phi_j(\eta)\left(\overline{\beta}_{1j}^{x}+\frac{\overline{\beta}_{4j}^{x}-\overline{\beta}_{1j}^{x}}{2}(\xi+1)\right) \tag{16}$$

$$y(\xi,\eta)=\sum_{\mathrm{i}=1}^{4}L_i(\xi)\left(y_{i0}+\frac{y_{im}-y_{i0}}{m_s}\eta\right) \tag{17}$$

where the coefficients $\overline{\beta}_{1j}^{x}$ and $\overline{\beta}_{4j}^{x}$ refer to the first and forth nodal line only, i.e. the external nodal lines, and y_{i0} and y_{im} are the *y*-coordinates of the starting and ending nodes, respectively, of each nodal line.

Taking the derivatives of (16) and (17), the components of the Jacobian matrix, **J**, of the transformation can be expressed by

$$\begin{bmatrix}\frac{\partial\xi}{\partial x} & \frac{\partial\eta}{\partial x}\\ \frac{\partial\xi}{\partial y} & \frac{\partial\eta}{\partial y}\end{bmatrix}=\begin{bmatrix}\frac{\partial x}{\partial\xi} & \frac{\partial y}{\partial\xi}\\ \frac{\partial x}{\partial\eta} & \frac{\partial y}{\partial\eta}\end{bmatrix}^{-1}=\mathbf{J}^{-\mathrm{T}} \tag{18}$$

where

$$\frac{\partial x(\xi,\eta)}{\partial\xi}=\sum_{j=-1}^{m+1}\left(\phi_j(\eta)\cdot\frac{\overline{\beta}_{4j}^{x}-\overline{\beta}_{1j}^{x}}{2}\right) \tag{19}$$

$$\frac{\partial x(\xi,\eta)}{\partial\eta}=\sum_{j=-1}^{m+1}\phi_j'(\eta)\left(\overline{\beta}_{1j}^{x}+\frac{\overline{\beta}_{4j}^{x}-\overline{\beta}_{1j}^{x}}{2}(\xi+1)\right) \tag{20}$$

$$\frac{\partial y(\xi,\eta)}{\partial\xi}=\sum_{\mathrm{i}=1}^{4}L_i'(\xi)\left(y_{i0}+\frac{y_{im}-y_{i0}}{m}\eta\right) \tag{21}$$

$$\frac{\partial y(\xi,\eta)}{\partial\eta}=\sum_{\mathrm{i}=1}^{4}\left(L_i(\xi)\cdot\frac{y_{im}-y_{i0}}{m}\right) \tag{22}$$

where the prime symbol on the shape functions indicates the total derivative, i.e.

$$L_i'(\xi)=\frac{dL_i(\xi)}{d\xi} \tag{23}$$

$$\phi_j'(\eta)=\frac{d\phi_j(\eta)}{d\eta} \tag{24}$$

Displacement functions

The actual three-dimensional thin-walled structure is modelled as a folded two-dimensional structure, i.e. as an assembly of flat plates. Consequently, the displacement field consists of a set of two-dimensional functions defined on the

mid-surface. Fig. 4 illustrates a general mid-surface of a plate, the local and global coordinate systems and the displacement functions associated with these systems.

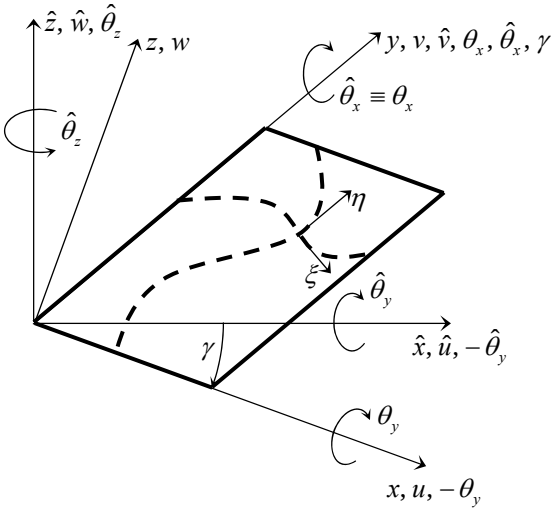

Fig. 4: Coordinate systems and kinematics functions.

Within each plate assembly, five generalized displacement functions are defined: the two in-plane displacements, u and v, the out-of-plane displacement, w, and the two rotations, θ_x and θ_y. According to the Mindlin plate theory, the total displacement field, $\overline{u}$, $\overline{v}$, $\overline{w}$ at the general point, (x, y, z), is given by

$$\overline{u}(x, y, z) = u(x, y) + z\,\theta_x(x, y) \tag{25}$$

$$\overline{v}(x, y, z) = v(x, y) + z\,\theta_y(x, y) \tag{26}$$

$$\overline{w}(x, y, z) = w(x, y) \tag{27}$$

The five generalized displacement functions, u, v, w, θ_x and θ_y, which according to (25), (26) and, (27) describe the displacement field of a plate of constant thickness, t, can be expressed in terms of the curvilinear coordinate system by the Lagrangian shape and B_3-spline functions as follows

$$\delta(\xi, \eta) = \sum_{i=1}^{4} \sum_{j=-1}^{m+1} L_i(\xi)\,\phi_j(\eta)\,\alpha_{ij}^{\delta} \tag{28}$$

where δ represents the generic generalized displacement function and may assume the values u, v, w, θ_x and θ_y. The numerical coefficients α_{ij}^{δ} represent the generalized variables of the problem.

Introducing now the shape function N_{ij} as

$$N_{ij}(\xi, \eta) = L_i(\xi)\,\phi_j(\eta) \tag{29}$$

a compact formulation of the general displacement function is given by

$$\delta(\xi,\eta)=\sum_{i=1}^{4}\sum_{j=-1}^{m+1}N_{ij}(\xi,\eta)\,\alpha_{ij}^{\delta} \tag{30}$$

It is convenient to introduce the matrix formulation for the displacement field vector $\boldsymbol{\delta}$ as follows

$$\boldsymbol{\delta}=\mathbf{N}\,\boldsymbol{\alpha} \tag{31}$$

where

$$\boldsymbol{\delta}=\boldsymbol{\delta}(\xi,\eta)=\begin{bmatrix} u(\xi,\eta)\\ v(\xi,\eta)\\ w(\xi,\eta)\\ \theta_x(\xi,\eta)\\ \theta_y(\xi,\eta)\end{bmatrix} \tag{32}$$

$$\mathbf{N}=\begin{bmatrix}\mathbf{N}_1\mathbf{I}_5 & \mathbf{N}_2\mathbf{I}_5 & \mathbf{N}_3\mathbf{I}_5 & \mathbf{N}_4\mathbf{I}_5\end{bmatrix} \tag{33}$$

$$\boldsymbol{\alpha}=\begin{bmatrix}\boldsymbol{\alpha}_1^{uT} & \boldsymbol{\alpha}_1^{vT} & \boldsymbol{\alpha}_1^{wT} & \boldsymbol{\alpha}_1^{\theta_x T} & \boldsymbol{\alpha}_1^{\theta_y T} & \cdots & \boldsymbol{\alpha}_4^{uT} & \boldsymbol{\alpha}_4^{vT} & \boldsymbol{\alpha}_4^{wT} & \boldsymbol{\alpha}_4^{\theta_x T} & \boldsymbol{\alpha}_4^{\theta_y T}\end{bmatrix}^T \tag{34}$$

where the i^{th} sub-matrix $\mathbf{N}_i$ and the sub-vector $\boldsymbol{\alpha}_i^{\delta}$ are given by

$$\mathbf{N}_i=L_i(\xi)\begin{bmatrix}\phi_{-1}(\eta) & \phi_0(\eta) & \phi_1(\eta) & \cdots & \phi_m(\eta) & \phi_{m+1}(\eta)\end{bmatrix} \tag{35}$$

$$\boldsymbol{\alpha}_i^{\delta T}=\begin{bmatrix}\alpha_{i\,-1}^{\delta} & \alpha_{i\,0}^{\delta} & \alpha_{i\,1}^{\delta} & \cdots & \alpha_{i\,m}^{\delta} & \alpha_{i\,m+1}^{\delta}\end{bmatrix} \tag{36}$$

and $\mathbf{I}_5$ represents the identity matrix of order five.

Strain-displacements relations

The full second-order strain-displacement relations are utilized in the elastic nonlinear analysis. To define the deformation of a thin-walled prismatic structure under large displacements, the contributions from both the in-plane and out-of-plane displacements to the strains are taken into account. Local buckling deformations may be captured from the second order terms related to the out-of-plane displacement, as in the plate buckling analysis. Distortional buckling, typical of stiffened thin-walled structures, can only be captured if the second order terms related to in-plane displacements are included in the strain-displacement relations. Generally speaking, the contributions from the

longitudinal displacement are of secondary importance and can usually be ignored. They have nevertheless been considered in the present work.

Initial imperfections may significantly affect the load-displacement response, even in the early stage of loading. They are represented by the terms u_0, v_0 and w_0 and introduced in the strain-displacement nonlinear relations.

The formulation here presented assumes large deformations but small rotations. The curvature-displacement relations are consequently taken in their linear form.

The general strain-displacement relation is given by

$$\varepsilon_{ij} = \frac{1}{2}\left(u_{i,j} + u_{j,i} - u_{0i,j} - u_{0j,i}\right) + \frac{1}{2}\sum_k \left[\left(u_{k,i}\, u_{k,j}\right) - \left(u_{0k,i}\, u_{0k,j}\right)\right] \tag{37}$$

The strain components at the mid-surface are

$$\varepsilon_x = \frac{\partial u}{\partial x} - \frac{\partial u_0}{\partial x} + \frac{1}{2}\left[\left(\frac{\partial u}{\partial x}\right)^2 + \left(\frac{\partial v}{\partial x}\right)^2 + \left(\frac{\partial w}{\partial x}\right)^2 - \left(\frac{\partial u_0}{\partial x}\right)^2 - \left(\frac{\partial v_0}{\partial x}\right)^2 - \left(\frac{\partial w_0}{\partial x}\right)^2\right] \tag{38}$$

$$\varepsilon_y = \frac{\partial v}{\partial y} - \frac{\partial v_0}{\partial y} + \frac{1}{2}\left[\left(\frac{\partial u}{\partial y}\right)^2 + \left(\frac{\partial v}{\partial y}\right)^2 + \left(\frac{\partial w}{\partial y}\right)^2 - \left(\frac{\partial u_0}{\partial y}\right)^2 - \left(\frac{\partial v_0}{\partial y}\right)^2 - \left(\frac{\partial w_0}{\partial y}\right)^2\right] \tag{39}$$

$$\gamma_{xy} = \frac{\partial u}{\partial y} + \frac{\partial v}{\partial x} - \frac{\partial u_0}{\partial y} - \frac{\partial v_0}{\partial x} + \left[\frac{\partial u}{\partial x}\frac{\partial u}{\partial y} + \frac{\partial v}{\partial x}\frac{\partial v}{\partial y} + \frac{\partial w}{\partial x}\frac{\partial w}{\partial y} - \frac{\partial u_0}{\partial x}\frac{\partial u_0}{\partial y} - \frac{\partial v_0}{\partial x}\frac{\partial v_0}{\partial y} - \frac{\partial w_0}{\partial x}\frac{\partial w_0}{\partial y}\right] \tag{40}$$

$$\gamma_{xz} = \frac{\partial u}{\partial z} + \frac{\partial w}{\partial x} - \frac{\partial u_0}{\partial z} - \frac{\partial w_0}{\partial x} + \left[\frac{\partial u}{\partial x}\frac{\partial u}{\partial z} + \frac{\partial v}{\partial x}\frac{\partial v}{\partial z} - \frac{\partial u_0}{\partial x}\frac{\partial u_0}{\partial z} - \frac{\partial v_0}{\partial x}\frac{\partial v_0}{\partial z}\right] \tag{41}$$

$$\gamma_{yz} = \frac{\partial v}{\partial z} + \frac{\partial w}{\partial y} - \frac{\partial v_0}{\partial z} - \frac{\partial w_0}{\partial y} + \left[\frac{\partial u}{\partial y}\frac{\partial u}{\partial z} + \frac{\partial v}{\partial y}\frac{\partial v}{\partial z} - \frac{\partial u_0}{\partial y}\frac{\partial u_0}{\partial z} - \frac{\partial v_0}{\partial y}\frac{\partial v_0}{\partial z}\right] \tag{42}$$

In (41) and (42), the nonlinear terms in the partial derivatives of the out-of-plane displacement with respect to the through-thickness coordinate, $\partial w/\partial z$ and $\partial w_0/\partial z$, are omitted because they vanish according to (27).

The curvature-displacement relations are expressed by

$$\chi_x = \frac{\partial \theta_x}{\partial x} - \frac{\partial \theta_{x0}}{\partial x} \tag{43}$$

$$\chi_y = \frac{\partial \theta_y}{\partial y} - \frac{\partial \theta_{y0}}{\partial y} \tag{44}$$

$$\chi_{xy} = \frac{\partial \theta_x}{\partial y} + \frac{\partial \theta_y}{\partial x} - \frac{\partial \theta_{x0}}{\partial y} - \frac{\partial \theta_{y0}}{\partial x} \tag{45}$$

We may note that the strain-displacement relations here presented involve only first order derivatives in the local coordinates x, y and z. Developing the derivative of the general displacement function δ with respect to x we have

$$\frac{\partial \delta(\xi,\eta)}{\partial x} = \frac{\partial \delta(\xi,\eta)}{\partial \xi}\frac{\partial \xi}{\partial x} + \frac{\partial \delta(\xi,\eta)}{\partial \eta}\frac{\partial \eta}{\partial x} \tag{46}$$

Introducing (30) in (46) yields

$$\begin{aligned}\frac{\partial \delta(\xi,\eta)}{\partial x} &= \sum_{i=1}^{4}\sum_{j=-1}^{m+1} L_i'(\xi)\,\phi_j(\eta)\,\alpha_{ij}^{\delta}\,\frac{\partial \xi}{\partial x} + \sum_{i=1}^{4}\sum_{j=-1}^{m+1} L_i(\xi)\,\phi_j'(\eta)\,\alpha_{ij}^{\delta}\,\frac{\partial \eta}{\partial x} \\ &= \sum_{i=1}^{4}\sum_{j=-1}^{m+1}\left(L_i'(\xi)\,\phi_j(\eta)\frac{\partial \xi}{\partial x} + L_i(\xi)\,\phi_j'(\eta)\frac{\partial \eta}{\partial x}\right)\alpha_{ij}^{\delta}\end{aligned} \tag{47}$$

Similarly, for the derivative with respect to y we obtain

$$\frac{\partial \delta(\xi,\eta)}{\partial y} = \sum_{i=1}^{4}\sum_{j=-1}^{m+1}\left(L_i'(\xi)\,\phi_j(\eta)\frac{\partial \xi}{\partial y} + L_i(\xi)\,\phi_j'(\eta)\frac{\partial \eta}{\partial y}\right)\alpha_{ij}^{\delta} \tag{48}$$

By introducing the definitions

$$B_{ij,x}(\xi,\eta) = L_i'(\xi)\,\phi_j(\eta)\frac{\partial \xi}{\partial x} + L_i(\xi)\,\phi_j'(\eta)\frac{\partial \eta}{\partial x} \tag{49}$$

$$B_{ij,y}(\xi,\eta) = L_i'(\xi)\,\phi_j(\eta)\frac{\partial \xi}{\partial y} + L_i(\xi)\,\phi_j'(\eta)\frac{\partial \eta}{\partial y} \tag{50}$$

it follows that (49) and (50) can be compactly rewritten as

$$\frac{\partial \delta(\xi,\eta)}{\partial x} = \sum_{i=1}^{4}\sum_{j=-1}^{m+1} B_{ij,x}(\xi,\eta)\,\alpha_{ij}^{\delta} \tag{51}$$

$$\frac{\partial \delta(\xi,\eta)}{\partial y} = \sum_{i=1}^{4}\sum_{j=-1}^{m+1} B_{ij,y}(\xi,\eta)\,\alpha_{ij}^{\delta} \tag{52}$$

Considering now the derivatives of the displacement field with respect to the through-thickness coordinate z we observe from (25) and (26) that they reduce to the expressions in the two in-plane rotations θ_x and θ_y. For a consistent notation we may nevertheless write them generically as

$$\frac{\partial \delta(\xi,\eta)}{\partial z} = \sum_{i=1}^{4}\sum_{j=-1}^{m+1} B_{ij,z}(\xi,\eta)\,\alpha_{ij}^{\delta} \tag{53}$$

where the function $B_{ij,z}(\xi,\eta)$ is simply expressed by

$$B_{ij,z}(\xi,\eta) = N_{ij}(\xi,\eta) = L_i(\xi,\eta)\,\phi_j(\eta) \tag{54}$$

It is convenient introduce a vector form for (51), (52) and (53)

$$\frac{\partial\delta(\xi,\eta)}{\partial x} = \mathbf{B}_{\delta x}\,\boldsymbol{\alpha} \tag{55}$$

$$\frac{\partial\delta(\xi,\eta)}{\partial y} = \mathbf{B}_{\delta y}\,\boldsymbol{\alpha} \tag{56}$$

$$\frac{\partial\delta(\xi,\eta)}{\partial z} = \mathbf{B}_{\delta z}\,\boldsymbol{\alpha} \tag{57}$$

The basic strain vectors $\mathbf{B}_{\delta x}$, $\mathbf{B}_{\delta y}$ and $\mathbf{B}_{\delta z}$ are row vectors of the same length as the coefficient vector $\boldsymbol{\alpha}$ introduced in (34). They are expressed by

$$\mathbf{B}_{ux} = \left[\mathbf{B}_x^1\ \mathbf{0}\ \mathbf{0}\ \mathbf{0}\ \mathbf{0}\ \mathbf{B}_x^2\ \mathbf{0}\ \mathbf{0}\ \mathbf{0}\ \mathbf{0}\ \mathbf{B}_x^3\ \mathbf{0}\ \mathbf{0}\ \mathbf{0}\ \mathbf{0}\ \mathbf{B}_x^4\ \mathbf{0}\ \mathbf{0}\ \mathbf{0}\ \mathbf{0}\right] \tag{58}$$

$$\mathbf{B}_{uy} = \left[\mathbf{B}_y^1\ \mathbf{0}\ \mathbf{0}\ \mathbf{0}\ \mathbf{0}\ \mathbf{B}_y^2\ \mathbf{0}\ \mathbf{0}\ \mathbf{0}\ \mathbf{0}\ \mathbf{B}_y^3\ \mathbf{0}\ \mathbf{0}\ \mathbf{0}\ \mathbf{0}\ \mathbf{B}_y^4\ \mathbf{0}\ \mathbf{0}\ \mathbf{0}\ \mathbf{0}\right] \tag{59}$$

$$\mathbf{B}_{uz} = \left[\mathbf{0}\ \mathbf{0}\ \mathbf{0}\ \mathbf{B}_z^1\ \mathbf{0}\ \mathbf{0}\ \mathbf{0}\ \mathbf{0}\ \mathbf{B}_z^2\ \mathbf{0}\ \mathbf{0}\ \mathbf{0}\ \mathbf{0}\ \mathbf{B}_z^3\ \mathbf{0}\ \mathbf{0}\ \mathbf{0}\ \mathbf{0}\ \mathbf{B}_z^4\ \mathbf{0}\right] \tag{60}$$

$$\mathbf{B}_{vx} = \left[\mathbf{0}\ \mathbf{B}_x^1\ \mathbf{0}\ \mathbf{0}\ \mathbf{0}\ \mathbf{0}\ \mathbf{B}_x^2\ \mathbf{0}\ \mathbf{0}\ \mathbf{0}\ \mathbf{0}\ \mathbf{B}_x^3\ \mathbf{0}\ \mathbf{0}\ \mathbf{0}\ \mathbf{0}\ \mathbf{B}_x^4\ \mathbf{0}\ \mathbf{0}\ \mathbf{0}\right] \tag{61}$$

$$\mathbf{B}_{vy} = \left[\mathbf{0}\ \mathbf{B}_y^1\ \mathbf{0}\ \mathbf{0}\ \mathbf{0}\ \mathbf{0}\ \mathbf{B}_y^2\ \mathbf{0}\ \mathbf{0}\ \mathbf{0}\ \mathbf{0}\ \mathbf{B}_y^3\ \mathbf{0}\ \mathbf{0}\ \mathbf{0}\ \mathbf{0}\ \mathbf{B}_y^4\ \mathbf{0}\ \mathbf{0}\ \mathbf{0}\right] \tag{62}$$

$$\mathbf{B}_{vz} = \left[\mathbf{0}\ \mathbf{0}\ \mathbf{0}\ \mathbf{0}\ \mathbf{B}_z^1\ \mathbf{0}\ \mathbf{0}\ \mathbf{0}\ \mathbf{0}\ \mathbf{B}_z^2\ \mathbf{0}\ \mathbf{0}\ \mathbf{0}\ \mathbf{0}\ \mathbf{B}_z^3\ \mathbf{0}\ \mathbf{0}\ \mathbf{0}\ \mathbf{0}\ \mathbf{B}_z^4\right] \tag{63}$$

$$\mathbf{B}_{wx} = \left[\mathbf{0}\ \mathbf{0}\ \mathbf{B}_x^1\ \mathbf{0}\ \mathbf{0}\ \mathbf{0}\ \mathbf{0}\ \mathbf{B}_x^2\ \mathbf{0}\ \mathbf{0}\ \mathbf{0}\ \mathbf{0}\ \mathbf{B}_x^3\ \mathbf{0}\ \mathbf{0}\ \mathbf{0}\ \mathbf{0}\ \mathbf{B}_x^4\ \mathbf{0}\ \mathbf{0}\right] \tag{64}$$

$$\mathbf{B}_{wy} = \left[\mathbf{0}\ \mathbf{0}\ \mathbf{B}_y^1\ \mathbf{0}\ \mathbf{0}\ \mathbf{0}\ \mathbf{0}\ \mathbf{B}_y^2\ \mathbf{0}\ \mathbf{0}\ \mathbf{0}\ \mathbf{0}\ \mathbf{B}_y^3\ \mathbf{0}\ \mathbf{0}\ \mathbf{0}\ \mathbf{0}\ \mathbf{B}_y^4\ \mathbf{0}\ \mathbf{0}\right] \tag{65}$$

$$\mathbf{B}_{\theta_x x} = \left[\mathbf{0}\ \mathbf{0}\ \mathbf{0}\ \mathbf{B}_x^1\ \mathbf{0}\ \mathbf{0}\ \mathbf{0}\ \mathbf{0}\ \mathbf{B}_x^2\ \mathbf{0}\ \mathbf{0}\ \mathbf{0}\ \mathbf{0}\ \mathbf{B}_x^3\ \mathbf{0}\ \mathbf{0}\ \mathbf{0}\ \mathbf{0}\ \mathbf{B}_x^4\ \mathbf{0}\right] \tag{66}$$

$$\mathbf{B}_{\theta_x y} = \left[\mathbf{0}\ \mathbf{0}\ \mathbf{0}\ \mathbf{B}_y^1\ \mathbf{0}\ \mathbf{0}\ \mathbf{0}\ \mathbf{0}\ \mathbf{B}_y^2\ \mathbf{0}\ \mathbf{0}\ \mathbf{0}\ \mathbf{0}\ \mathbf{B}_y^3\ \mathbf{0}\ \mathbf{0}\ \mathbf{0}\ \mathbf{0}\ \mathbf{B}_y^4\ \mathbf{0}\right] \tag{67}$$

$$\mathbf{B}_{\theta_y x} = \left[\mathbf{0}\ \mathbf{0}\ \mathbf{0}\ \mathbf{0}\ \mathbf{B}_x^1\ \mathbf{0}\ \mathbf{0}\ \mathbf{0}\ \mathbf{0}\ \mathbf{B}_x^2\ \mathbf{0}\ \mathbf{0}\ \mathbf{0}\ \mathbf{0}\ \mathbf{B}_x^3\ \mathbf{0}\ \mathbf{0}\ \mathbf{0}\ \mathbf{0}\ \mathbf{B}_x^4\right] \tag{68}$$

$$\mathbf{B}_{\theta_y y} = \left[\mathbf{0}\ \mathbf{0}\ \mathbf{0}\ \mathbf{0}\ \mathbf{B}_y^1\ \mathbf{0}\ \mathbf{0}\ \mathbf{0}\ \mathbf{0}\ \mathbf{B}_y^2\ \mathbf{0}\ \mathbf{0}\ \mathbf{0}\ \mathbf{0}\ \mathbf{B}_y^3\ \mathbf{0}\ \mathbf{0}\ \mathbf{0}\ \mathbf{0}\ \mathbf{B}_y^4\right] \tag{69}$$

The generic sub-vectors $\mathbf{B}_x^i$, $\mathbf{B}_y^i$ and $\mathbf{B}_z^i$ are the full set of m+3 functions given in (55), (56) and (57) referring to the i^{th} nodal line, i.e.

$$\mathbf{B}_x^i = \mathbf{B}_x^i(\xi,\eta) = \left[B_{i-1,x}(\xi,\eta)\ B_{i0,x}(\xi,\eta)\ B_{i1,x}(\xi,\eta)\cdots B_{im,x}(\xi,\eta)\ B_{im+1,x}(\xi,\eta)\right] \tag{70}$$

$$\mathbf{B}_y^i = \mathbf{B}_y^i(\xi,\eta) = \left[B_{i-1,y}(\xi,\eta)\ B_{i0,y}(\xi,\eta)\ B_{i1,y}(\xi,\eta)\cdots B_{im,y}(\xi,\eta)\ B_{im+1,y}(\xi,\eta)\right] \tag{71}$$

$$\mathbf{B}_z^i = \mathbf{B}_z^i(\xi,\eta) = \left[B_{i-1,z}(\xi,\eta)\ B_{i0,z}(\xi,\eta)\ B_{i1,z}(\xi,\eta) \cdots B_{im,z}(\xi,\eta)\ B_{im+1,z}(\xi,\eta) \right] \quad (72)$$

and the sub-vector **0** is a row vector of length m+3 with zero entries.

The relations expressed in (38) to (42) can now be written in the condensed form

$$\boldsymbol{\varepsilon} = \mathbf{B}\,\boldsymbol{\alpha} = \left[\mathbf{B}_L + \mathbf{B}_1(\boldsymbol{\alpha}) \right] \boldsymbol{\alpha} \quad (73)$$

where, $\boldsymbol{\varepsilon} = \left[\varepsilon_x\ \varepsilon_y\ \gamma_{xy}\ \gamma_{xz}\ \gamma_{yz}\ \chi_x\ \chi_y\ \chi_{xy} \right]^T$, $\mathbf{B}_L$ denotes the linear strain matrix and $\mathbf{B}_1(\boldsymbol{\alpha})$ is the nonlinear strain matrix, which is a function of the displacements, $\boldsymbol{\alpha}$. By using the definitions given by (58) to (69), the linear strain matrix can be written as

$$\mathbf{B}_L = \begin{bmatrix} \mathbf{B}_{ux} \\ \mathbf{B}_{vy} \\ \mathbf{B}_{uy} + \mathbf{B}_{vx} \\ \mathbf{B}_{uz} + \mathbf{B}_{wx} \\ \mathbf{B}_{vz} + \mathbf{B}_{wy} \\ \mathbf{B}_{\theta_x x} \\ \mathbf{B}_{\theta_y y} \\ \mathbf{B}_{\theta_x y} + \mathbf{B}_{\theta_y x} \end{bmatrix} \quad (74)$$

In the present report, the nonlinear equilibrium equations are solved by an iterative incremental method, i.e. by solving a converging series of linearised problems. The second-order strain matrix therefore has to be linearised. This can be achieved by using the coefficients obtained from the previous iteration step, $\boldsymbol{\alpha}_{prev}$. For example, the first second-order term in (38), $(\partial u/\partial x)^2$, can be expressed as

$$\left(\frac{\partial u(\boldsymbol{\alpha})}{\partial x} \right)^2 \cong \frac{\partial u(\boldsymbol{\alpha}_{prev})}{\partial x} \frac{\partial u(\boldsymbol{\alpha})}{\partial x} = u_{,x} \frac{\partial u(\boldsymbol{\alpha})}{\partial x} = u_{,x}\, \mathbf{B}_{ux}\, \boldsymbol{\alpha} \quad (75)$$

All the other second order terms can be similarly linearised and the second-order strain matrix $\mathbf{B}_1(\boldsymbol{\alpha})$ becomes

$$\mathbf{B}_1(\boldsymbol{\alpha}) \cong \mathbf{B}_1(\boldsymbol{\alpha}_{prev}) = \frac{1}{2}\begin{bmatrix} u_{,x}\,\mathbf{B}_{ux} + v_{,x}\,\mathbf{B}_{vx} + w_{,x}\,\mathbf{B}_{wx} \\ u_{,y}\,\mathbf{B}_{uy} + v_{,y}\,\mathbf{B}_{vy} + w_{,y}\,\mathbf{B}_{wy} \\ u_{,x}\,\mathbf{B}_{uy} + v_{,x}\,\mathbf{B}_{vy} + w_{,x}\,\mathbf{B}_{wy} \\ u_{,x}\,\mathbf{B}_{uz} + v_{,x}\,\mathbf{B}_{vz} + w_{,x}\,\mathbf{B}_{wz} \\ u_{,y}\,\mathbf{B}_{uz} + v_{,y}\,\mathbf{B}_{vz} + w_{,y}\,\mathbf{B}_{wz} \\ \mathbf{0} \\ \mathbf{0} \\ \mathbf{0} \end{bmatrix} \tag{76}$$

where $u_{,x}$, $u_{,y}$, $v_{,x}$, $v_{,y}$, $w_{,x}$ and $w_{,y}$ are the derivatives of the displacement functions evaluated by means of the solution vector $\boldsymbol{\alpha}_{prev}$. Taking the variation of (73) with respect to $\boldsymbol{\alpha}$ we obtain the incremental strain-displacement relation

$$\begin{aligned} d\boldsymbol{\varepsilon} &= \left[\mathbf{B}_L + \mathbf{B}_1(\boldsymbol{\alpha})\right] d\boldsymbol{\alpha} + \frac{d\mathbf{B}_1(\boldsymbol{\alpha})}{d\boldsymbol{\alpha}}\,\boldsymbol{\alpha}\, d\boldsymbol{\alpha} \\ &= \left[\mathbf{B}_L + 2\mathbf{B}_1(\boldsymbol{\alpha})\right] d\boldsymbol{\alpha} \\ &= \left[\mathbf{B}_L + \mathbf{B}_N(\boldsymbol{\alpha})\right] d\boldsymbol{\alpha} \\ &= \overline{\mathbf{B}}\, d\boldsymbol{\alpha} \end{aligned} \tag{77}$$

where we have introduced the nonlinear strain matrix $\mathbf{B}_N(\boldsymbol{\alpha}) = 2\mathbf{B}_1(\boldsymbol{\alpha})$ associated with the strain increment $d\boldsymbol{\varepsilon}$.

Stress-strain relations

In the present work we deal only with geometrical nonlinearity. The material constitutive equations are those of a hyper-elastic material, i.e.

$$\boldsymbol{\sigma} = \mathbf{D}\,\boldsymbol{\varepsilon} \tag{78}$$

For the purpose of clarity, we will separate the membrane, out-of-plane shear and flexural contributions:

$\boldsymbol{\sigma} = \begin{bmatrix} \boldsymbol{\sigma}_M \\ \boldsymbol{\sigma}_S \\ \boldsymbol{\sigma}_F \end{bmatrix}$, $\mathbf{D} = \begin{bmatrix} \mathbf{D}_M & \mathbf{0} & \mathbf{0} \\ \mathbf{0} & \mathbf{D}_S & \mathbf{0} \\ \mathbf{0} & \mathbf{0} & \mathbf{D}_F \end{bmatrix}$ and $\boldsymbol{\varepsilon} = \begin{bmatrix} \boldsymbol{\varepsilon}_M \\ \boldsymbol{\varepsilon}_S \\ \boldsymbol{\varepsilon}_F \end{bmatrix}$, where the subscript "*M*" stands for membrane, "*S*" for out-of-plane shear and "*F*" for flexural.

For the membrane part,

$$\boldsymbol{\sigma}_M = \begin{bmatrix} \sigma_x \\ \sigma_y \\ \tau_{xy} \end{bmatrix} \tag{79}$$

$$\mathbf{D}_M = \begin{bmatrix} D_M^x & D_M^1 & 0 \\ D_M^1 & D_M^y & 0 \\ 0 & 0 & D_M^{xy} \end{bmatrix} \tag{80}$$

$$\begin{cases} D_M^x = \dfrac{E_x}{1-\nu_x\nu_y} \\ D_M^y = \dfrac{E_y}{1-\nu_x\nu_y} \\ D_M^1 = \nu_x D_M^y = \nu_y D_M^x \\ D_M^{xy} = G_{xy} \end{cases} \tag{81}$$

$$\boldsymbol{\varepsilon}_M = \begin{bmatrix} \varepsilon_M \\ \varepsilon_y \\ \gamma_{xy} \end{bmatrix} \tag{82}$$

For the out-of-plane shear part,

$$\boldsymbol{\sigma}_S = \begin{bmatrix} \tau_{xz} \\ \tau_{yz} \end{bmatrix} \tag{83}$$

$$\mathbf{D}_S = \begin{bmatrix} D_S^{xz} & 0 \\ 0 & D_S^{yz} \end{bmatrix} \tag{84}$$

$$D_S^{xz} = D_S^{yz} = \frac{G_{xy}}{1.2} \tag{85}$$

$$\boldsymbol{\varepsilon}_S = \begin{bmatrix} \gamma_{xz} \\ \gamma_{yz} \end{bmatrix} \tag{86}$$

For the flexural part

$$\boldsymbol{\sigma}_F = \begin{bmatrix} m_x \\ m_y \\ m_{xy} \end{bmatrix} \tag{87}$$

$$\mathbf{D}_F = \begin{bmatrix} D_F^x & D_F^1 & 0 \\ D_F^1 & D_F^y & 0 \\ 0 & 0 & D_F^{xy} \end{bmatrix} \tag{88}$$

$$\begin{cases} D_F^x = \dfrac{E_x t^3}{12\left(1-\nu_x \nu_y\right)} \\ D_F^y = \dfrac{E_y t^3}{12\left(1-\nu_x \nu_y\right)} \\ D_F^1 = \nu_x D_F^y = \nu_y D_F^x \\ D_F^{xy} = \dfrac{G_{xy} t^3}{12} \end{cases} \tag{89}$$

$$\boldsymbol{\varepsilon}_F = \begin{bmatrix} \chi_x \\ \chi_y \\ \chi_{xy} \end{bmatrix} \tag{90}$$

where E_x and E_y, and ν_x and ν_y are the Young's moduli and Poisson's ratios in *x*-direction and *y*-direction, respectively, G_{xy} is the shear modulus and t is the thickness of the strip.

Equilibrium equations

The objective of the geometric nonlinear analysis is to produce a discrete series of equilibrium configurations for a set of externally applied loads or displacements. An equilibrium configuration cannot in general be found directly, but an iterative procedure refining the solution is required. Suitable definitions of equilibrium and incremental equilibrium are generally obtained in finite element and finite strip analysis formulations by invoking the principle of virtual work. The internal virtual work is given by

$$dw_i = \int_V \left(d\boldsymbol{\varepsilon}^T\ \boldsymbol{\sigma}\right) dV = d\boldsymbol{\alpha}^T \int_V \left(\overline{\mathbf{B}}^{\ T}\ \boldsymbol{\sigma}\right) dV \tag{91}$$

while the external work can be expressed in matrix form as

$$dw_e = \int_V \left(d\boldsymbol{\delta}^T\ \mathbf{f}_e\right) dV = d\boldsymbol{\alpha}^T \int_V \left(\mathbf{N}^T\ \mathbf{f}_e\right) dV = d\boldsymbol{\alpha}^T\ \mathbf{f} \tag{92}$$

where $\mathbf{f}_e$ is the external load vector, $\mathbf{f}$ the so called equivalent load vector and V the volume of the strip. The equilibrium condition is given by

$$dw_i = dw_e \tag{93}$$

Defining the function $\boldsymbol{\Psi}(\boldsymbol{\alpha})$ as

$$\boldsymbol{\Psi}(\boldsymbol{\alpha}) = \int_V \left(\bar{\mathbf{B}}^{\,T}\,\boldsymbol{\sigma}\right) dV - \mathbf{f} \tag{94}$$

the static equilibrium condition stated in (93) is achieved when the function $\boldsymbol{\Psi}(\boldsymbol{\alpha})$ is equal to zero,

$$\boldsymbol{\Psi}(\boldsymbol{\alpha}) = \mathbf{0} \tag{95}$$

This is never exactly satisfied in a numerical analysis, and hence an appropriate convergence criterion has to be established. From (73) and (78)

$$\boldsymbol{\sigma} = \mathbf{D}\,\boldsymbol{\varepsilon} = \mathbf{D}\,\mathbf{B}\,\boldsymbol{\alpha} = \mathbf{D}\left[\mathbf{B}_L + \mathbf{B}_1(\boldsymbol{\alpha})\right]\boldsymbol{\alpha} \tag{96}$$

From (77)

$$\bar{\mathbf{B}} = \left[\mathbf{B}_L + \mathbf{B}_N(\boldsymbol{\alpha})\right] \tag{97}$$

Hence the first part of (94) may be written as

$$\begin{aligned}\int_V \left(\bar{\mathbf{B}}^{\,T}\,\boldsymbol{\sigma}\right) dV &= \int_V \left(\left[\mathbf{B}_L + \mathbf{B}_N(\boldsymbol{\alpha})\right]^{\,T}\,\mathbf{D}\left[\mathbf{B}_L + \mathbf{B}_1(\alpha)\right]\right) dV\,\boldsymbol{\alpha} \\ &= \mathbf{K}_E\,\boldsymbol{\alpha}\end{aligned} \tag{98}$$

where $\mathbf{K}_E$ is the so-called secant stiffness matrix given by

$$\begin{aligned}\mathbf{K}_E = &\int_V \left(\mathbf{B}_L^T\,\mathbf{D}\,\mathbf{B}_L\right) dV + \int_V \left(\mathbf{B}_L^T\,\mathbf{D}\,\mathbf{B}_1(\boldsymbol{\alpha})\right) dV + \\ &+ \int_V \left(\mathbf{B}_N(\boldsymbol{\alpha})^T\,\mathbf{D}\,\mathbf{B}_L\right) dV + \int_V \left(\mathbf{B}_N(\boldsymbol{\alpha})^T\,\mathbf{D}\,\mathbf{B}_1(\boldsymbol{\alpha})\right) dV\end{aligned} \tag{99}$$

The function $\boldsymbol{\Psi}(\boldsymbol{\alpha})$ can be regarded as an out-of-balance force vector, i.e. the difference between the equivalent external force vector and the corresponding nodal force vector produced by the internal stresses. It can be written in a condensed form as

$$\boldsymbol{\Psi}(\boldsymbol{\alpha}) = \mathbf{K}_E\,\boldsymbol{\alpha} - \mathbf{f} \tag{100}$$

By taking the variation of $\boldsymbol{\Psi}(\boldsymbol{\alpha})$ with respect to $\boldsymbol{\alpha}$ we obtain the tangential stiffness of the structure at a given displacement,

$$d\boldsymbol{\Psi}(\boldsymbol{\alpha}) = d\left(\int_V \left(\overline{\mathbf{B}}^{\,T}\,\boldsymbol{\sigma}\right) dV - \mathbf{f}\right) = \int_V \left(d\overline{\mathbf{B}}^{\,T}\,\boldsymbol{\sigma} + \overline{\mathbf{B}}^{\,T}\,d\boldsymbol{\sigma}\right) dV - d\mathbf{f} \tag{101}$$

In the first term of (101), $d\overline{\mathbf{B}}$ reduces to

$$d\overline{\mathbf{B}} = d\left[\mathbf{B}_L + \mathbf{B}_N(\boldsymbol{\alpha})\right] = d\mathbf{B}_N(\boldsymbol{\alpha}) \tag{102}$$

From (77) and (96) $d\boldsymbol{\sigma}$ is

$$d\boldsymbol{\sigma} = d\left(\mathbf{D}\,\boldsymbol{\varepsilon}\right) = \mathbf{D}\,d\boldsymbol{\varepsilon} = \mathbf{D}\,\overline{\mathbf{B}}\,d\boldsymbol{\alpha} \tag{103}$$

Therefore

$$d\boldsymbol{\Psi}(\boldsymbol{\alpha}) = \int_V \left(d\mathbf{B}_N(\boldsymbol{\alpha})^{\,T}\,\boldsymbol{\sigma}\right) dV + \int_V \left(\overline{\mathbf{B}}^{\,T}\,\mathbf{D}\,\overline{\mathbf{B}}\right) dV\; d\boldsymbol{\alpha} - d\mathbf{f} \tag{104}$$

From (76) and (77)

$$\mathbf{B}_N(\boldsymbol{\alpha}) = \begin{bmatrix} \dfrac{\partial u(\boldsymbol{\alpha})}{\partial x}\mathbf{B}_{ux} + \dfrac{\partial v(\boldsymbol{\alpha})}{\partial x}\mathbf{B}_{vx} + \dfrac{\partial w(\boldsymbol{\alpha})}{\partial x}\mathbf{B}_{wx} \\ \dfrac{\partial u(\boldsymbol{\alpha})}{\partial y}\mathbf{B}_{uy} + \dfrac{\partial v(\boldsymbol{\alpha})}{\partial y}\mathbf{B}_{vy} + \dfrac{\partial w(\boldsymbol{\alpha})}{\partial y}\mathbf{B}_{wy} \\ \dfrac{\partial u(\boldsymbol{\alpha})}{\partial x}\mathbf{B}_{uy} + \dfrac{\partial v(\boldsymbol{\alpha})}{\partial x}\mathbf{B}_{vy} + \dfrac{\partial w(\boldsymbol{\alpha})}{\partial x}\mathbf{B}_{wy} \\ \dfrac{\partial u(\boldsymbol{\alpha})}{\partial x}\mathbf{B}_{uz} + \dfrac{\partial v(\boldsymbol{\alpha})}{\partial x}\mathbf{B}_{vz} + \dfrac{\partial w(\boldsymbol{\alpha})}{\partial x}\mathbf{B}_{wz} \\ \dfrac{\partial u(\boldsymbol{\alpha})}{\partial y}\mathbf{B}_{uz} + \dfrac{\partial v(\boldsymbol{\alpha})}{\partial y}\mathbf{B}_{vz} + \dfrac{\partial w(\boldsymbol{\alpha})}{\partial y}\mathbf{B}_{wz} \\ \mathbf{0} \\ \mathbf{0} \\ \mathbf{0} \end{bmatrix} \tag{105}$$

Recalling (55), (56) and (57)

$$\mathbf{B}_N(\boldsymbol{\alpha}) = \boldsymbol{\alpha}^T \begin{bmatrix} \mathbf{B}_{ux}^T \mathbf{B}_{ux} + \mathbf{B}_{vx}^T \mathbf{B}_{vx} + \mathbf{B}_{wx}^T \mathbf{B}_{wx} \\ \mathbf{B}_{uy}^T \mathbf{B}_{uy} + \mathbf{B}_{vy}^T \mathbf{B}_{vy} + \mathbf{B}_{wy}^T \mathbf{B}_{wy} \\ \mathbf{B}_{ux}^T \mathbf{B}_{uy} + \mathbf{B}_{vx}^T \mathbf{B}_{vy} + \mathbf{B}_{wx}^T \mathbf{B}_{wy} \\ \mathbf{B}_{ux}^T \mathbf{B}_{uz} + \mathbf{B}_{vx}^T \mathbf{B}_{vz} + \mathbf{B}_{wx}^T \mathbf{B}_{wz} \\ \mathbf{B}_{uy}^T \mathbf{B}_{uz} + \mathbf{B}_{vy}^T \mathbf{B}_{vz} + \mathbf{B}_{wy}^T \mathbf{B}_{wz} \\ \mathbf{0} \\ \mathbf{0} \\ \mathbf{0} \end{bmatrix} \tag{106}$$

Hence $d\mathbf{B}_N(\boldsymbol{\alpha})$ is simply given by

$$d\mathbf{B}_N(\boldsymbol{\alpha}) = d\boldsymbol{\alpha}^T \begin{bmatrix} \mathbf{B}_{ux}^T \mathbf{B}_{ux} + \mathbf{B}_{vx}^T \mathbf{B}_{vx} + \mathbf{B}_{wx}^T \mathbf{B}_{wx} \\ \mathbf{B}_{uy}^T \mathbf{B}_{uy} + \mathbf{B}_{vy}^T \mathbf{B}_{vy} + \mathbf{B}_{wy}^T \mathbf{B}_{wy} \\ \mathbf{B}_{ux}^T \mathbf{B}_{uy} + \mathbf{B}_{vx}^T \mathbf{B}_{vy} + \mathbf{B}_{wx}^T \mathbf{B}_{wy} \\ \mathbf{B}_{ux}^T \mathbf{B}_{uz} + \mathbf{B}_{vx}^T \mathbf{B}_{vz} + \mathbf{B}_{wx}^T \mathbf{B}_{wz} \\ \mathbf{B}_{uy}^T \mathbf{B}_{uz} + \mathbf{B}_{vy}^T \mathbf{B}_{vz} + \mathbf{B}_{wy}^T \mathbf{B}_{wz} \\ \mathbf{0} \\ \mathbf{0} \\ \mathbf{0} \end{bmatrix} \tag{107}$$

The stress vector can be calculated according to (96) at a given $\boldsymbol{\alpha}_{prev}$ as

$$\boldsymbol{\sigma} \cong \boldsymbol{\sigma}(\boldsymbol{\alpha}_{prev}) = \mathbf{D}\left[\mathbf{B}_L + \mathbf{B}_1(\boldsymbol{\alpha}_{prev})\right]\boldsymbol{\alpha}_{prev} = \begin{bmatrix} \overline{\sigma}_x \\ \overline{\sigma}_y \\ \overline{\tau}_{xy} \\ \overline{\tau}_{xz} \\ \overline{\tau}_{yz} \\ \overline{m}_x \\ \overline{m}_y \\ \overline{m}_{xy} \end{bmatrix} \tag{108}$$

By (107) and (108), the first term in the right-hand side of (104) is

$$\int_V \left(d\mathbf{B}_N(\boldsymbol{\alpha})^T \boldsymbol{\sigma}\right) dV = \mathbf{K}_\sigma \, d\boldsymbol{\alpha} \tag{109}$$

where $\mathbf{K}_\sigma$ is the initial stress matrix given by

$$\begin{aligned}\mathbf{K}_\sigma = \int_V \Big[& \bar{\sigma}_x \left(\mathbf{B}_{ux}^T \mathbf{B}_{ux} + \mathbf{B}_{vx}^T \mathbf{B}_{vx} + \mathbf{B}_{wx}^T \mathbf{B}_{wx} \right) + \\ & + \bar{\sigma}_y \left(\mathbf{B}_{uy}^T \mathbf{B}_{uy} + \mathbf{B}_{vy}^T \mathbf{B}_{vy} + \mathbf{B}_{wy}^T \mathbf{B}_{wy} \right) + \\ & + \bar{\tau}_{xy} \left(\mathbf{B}_{ux}^T \mathbf{B}_{uy} + \mathbf{B}_{vx}^T \mathbf{B}_{vy} + \mathbf{B}_{wx}^T \mathbf{B}_{wy} \right) + \\ & + \bar{\tau}_{xz} \left(\mathbf{B}_{ux}^T \mathbf{B}_{uz} + \mathbf{B}_{vx}^T \mathbf{B}_{vz} + \mathbf{B}_{wx}^T \mathbf{B}_{wz} \right) + \\ & + \bar{\tau}_{yz} \left(\mathbf{B}_{uy}^T \mathbf{B}_{uz} + \mathbf{B}_{vy}^T \mathbf{B}_{vz} + \mathbf{B}_{wy}^T \mathbf{B}_{wz} \right) \Big] dV \end{aligned} \tag{110}$$

Developing the second term of (104) gives

$$\begin{aligned}\int_V \left(\bar{\mathbf{B}}^T \mathbf{D} \bar{\mathbf{B}} \right) dV &= \int_V \left(\left[\mathbf{B}_L + \mathbf{B}_N(\boldsymbol{\alpha}) \right]^T \mathbf{D} \left[\mathbf{B}_L + \mathbf{B}_N(\boldsymbol{\alpha}) \right] \right) dV = \\ &= \int_V \left(\mathbf{B}_L{}^T \mathbf{D} \mathbf{B}_L \right) dV + \int_V \left(\mathbf{B}_L{}^T \mathbf{D} \mathbf{B}_N(\boldsymbol{\alpha}) \right) dV + \\ &\quad + \int_V \left(\mathbf{B}_L{}^T \mathbf{D} \mathbf{B}_N(\boldsymbol{\alpha}) \right) dV + \int_V \left(\mathbf{B}_N(\boldsymbol{\alpha})^T \mathbf{D} \mathbf{B}_N(\boldsymbol{\alpha}) \right) dV \\ &= \mathbf{K}_L + \mathbf{K}_N \end{aligned} \tag{111}$$

where $\mathbf{K}_L$ is the conventional small displacement stiffness matrix and $\mathbf{K}_N$ is called the large displacement matrix. They are defined as

$$\mathbf{K}_L = \int_V \left(\mathbf{B}_L{}^T \mathbf{D} \mathbf{B}_L \right) dV \tag{112}$$

$$\begin{aligned}\mathbf{K}_N = & \int_V \left(\mathbf{B}_L{}^T \mathbf{D} \mathbf{B}_N(\boldsymbol{\alpha}) \right) dV + \int_V \left(\mathbf{B}_L{}^T \mathbf{D} \mathbf{B}_N(\boldsymbol{\alpha}) \right) dV + \\ & + \int_V \left(\mathbf{B}_N(\boldsymbol{\alpha})^T \mathbf{D} \mathbf{B}_N(\boldsymbol{\alpha}) \right) dV \end{aligned} \tag{113}$$

Equation (104) can finally be expressed as

$$d\boldsymbol{\Psi}(\boldsymbol{\alpha}) = \left(\mathbf{K}_L + \mathbf{K}_N + \mathbf{K}_\sigma \right) d\boldsymbol{\alpha} - d\mathbf{f} = \mathbf{K}_T \, d\boldsymbol{\alpha} - d\mathbf{f} \tag{114}$$

where $\mathbf{K}_T$ represents the total tangent stiffness matrix.

The integration procedure adopted in the present work for the calculation of the tangent matrix follows the usual finite element technique. A selective reduced numerical Gaussian integration has been adopted for reasons explained in Eccher et al. (2007a). The values of the functions $u_{,x}$, $u_{,y}$, $v_{,x}$, $v_{,y}$, $w_{,x}$ and $w_{,y}$ in (77) as well as those of the functions $\bar{\sigma}_x$, $\bar{\sigma}_y$, $\bar{\tau}_{xy}$, $\bar{\tau}_{xz}$ and $\bar{\tau}_{yz}$ in (110) are sampled at the Gaussian integration points and correspondingly utilized in the integration process.

Transformation to global coordinates

The relations presented in the previous sections refer to the local Cartesian coordinate system. In the case of a folded plate structure, those quantities have to be transformed into a global Cartesian coordinate system prior to proceeding with the assembly of the stiffness and stability matrices of the total structure. Fig. 4 shows a strip rotated by an angle γ with respect to the global coordinate systems $\hat{x}$-$\hat{y}$-$\hat{z}$. The matrix relating the generalized displacements in the local coordinate system, u, v, w, θ_x and θ_y, to the corresponding displacement functions in the global coordinate system, $\hat{u}$, $\hat{v}$, $\hat{w}$, $\hat{\theta}_x$ and $\hat{\theta}_y$ is given by

$$\hat{\boldsymbol{\delta}} = \begin{bmatrix} \hat{u} \\ \hat{v} \\ \hat{w} \\ \hat{\theta}_x \\ \hat{\theta}_y \end{bmatrix} = \begin{bmatrix} c & 0 & s & 0 & 0 \\ 0 & 1 & 0 & 0 & 0 \\ -s & 0 & c & 0 & 0 \\ 0 & 0 & 0 & 1 & 0 \\ 0 & 0 & 0 & 0 & 1 \end{bmatrix} \begin{bmatrix} u \\ v \\ w \\ \theta_x \\ \theta_y \end{bmatrix} = \mathbf{R}\,\boldsymbol{\delta} \tag{115}$$

where $c = \cos(\gamma)$ and $s = \sin(\gamma)$.

At fold lines between non-co-planar strips the local rotations equality θ_y of adjoining strips need to be transformed to global directions. That is, θ_y has to be separated into its two global components $\hat{\theta}_y$ and $\hat{\theta}_z$, i.e.

$$\tilde{\hat{\boldsymbol{\delta}}} = \begin{bmatrix} \hat{u} \\ \hat{v} \\ \hat{w} \\ \hat{\theta}_x \\ \hat{\theta}_y \\ \hat{\theta}_y \end{bmatrix} = \begin{bmatrix} c & 0 & s & 0 & 0 \\ 0 & 1 & 0 & 0 & 0 \\ -s & 0 & c & 0 & 0 \\ 0 & 0 & 0 & 1 & 0 \\ 0 & 0 & 0 & 0 & c \\ 0 & 0 & 0 & 0 & s \end{bmatrix} \begin{bmatrix} u \\ v \\ w \\ \theta_x \\ \theta_y \end{bmatrix} = \tilde{\hat{\mathbf{R}}}\,\boldsymbol{\delta} \tag{116}$$

Nonlinear solution technique

A general structural problem may involve complex equilibrium paths presenting pre- and post-critical paths characterized by hardening or softening behaviour, bifurcation points, and load and displacement limit points. A good nonlinear solver has, consequently, to be able to handle all these difficulties.

Many different techniques have been developed to solve nonlinear problems by means of iterative linearised methods. Some of the earliest

methods proposed, based on equilibrium iterations at a fixed load level, also known as Newton-Raphson methods, could trace pre- and post-critical paths but could not pass load limit points [18]. An alternative method based on displacement control [19] overcame this difficulty but conversely could not go past displacement limit points. More complex methods have been developed which combine load and displacement control, and are often referred to as generalized displacement control methods [20]. One of the most effective generalized displacement methods is the so called arc-length method which allows the load level to vary during the equilibrium iterations according to a prescribed constraint. Due to its flexibility and consistency, the latter has been adopted in the present work and is described in the following sections.

Solution technique

The method is based on an iterative-incremental strategy. Starting from an equilibrium configuration, $\boldsymbol{\alpha}_o$, where the subscript "*o*" stands for old, a finite load increment, $\Delta\mathbf{f}$, is applied and by iterating over load and displacement parameters, a new equilibrium condition, $\boldsymbol{\alpha}_n$, where the subscript "*n*" stands for new, is found.

The equilibrium condition (95) can be expressed in incremental form by expanding the out-of-balance force vector in a Taylor series as follows

$$\boldsymbol{\Psi}\left(\boldsymbol{\alpha}_n\right) = \boldsymbol{\Psi}\left(\boldsymbol{\alpha}_o + d\boldsymbol{\alpha}\right) \cong \boldsymbol{\Psi}\left(\boldsymbol{\alpha}_o\right) + \frac{\partial \boldsymbol{\Psi}\left(\boldsymbol{\alpha}_o\right)}{\partial \boldsymbol{\alpha}} d\boldsymbol{\alpha} \tag{117}$$

From (114) and utilizing that $\boldsymbol{\alpha}_o$ is an equilibrium configuration, i.e. $\boldsymbol{\Psi}\left(\boldsymbol{\alpha}_o\right) = \mathbf{0}$, the equilibrium condition (95) reduces to

$$\boldsymbol{\Psi}\left(\boldsymbol{\alpha}_n\right) \cong \mathbf{K}_T \, d\boldsymbol{\alpha} - d\mathbf{f} = \mathbf{0} \tag{118}$$

where $\mathbf{K}_T$ is the tangential stiffness matrix evaluated at $\boldsymbol{\alpha}_o$, $d\boldsymbol{\alpha}$ the displacement increment to be obtained and $d\mathbf{f}$ the load increment. For infinitesimally small load increments, $d\mathbf{f}$, by solving the linear system in (118), we can define the new equilibrium configuration $\left(\boldsymbol{\alpha}_n, \mathbf{f}_n\right)$ as

$$\boldsymbol{\alpha}_n = \boldsymbol{\alpha}_o + d\boldsymbol{\alpha} \tag{119}$$

$$\mathbf{f}_n = \mathbf{f}_o + d\mathbf{f} \tag{120}$$

In practical numerical procedures, the load increment is finite, $\Delta\mathbf{f}$, and generally expressed as

$$\Delta\mathbf{f} = \Delta\lambda_0 \mathbf{f} \tag{121}$$

where $\Delta\lambda_0$ is a scalar called the initial load increment.

The incremental displacement vector is obtained solving

$$\Delta\boldsymbol{\alpha} = \mathbf{K}_T^{-1}\,\Delta\mathbf{f} = \Delta\lambda_0\left(\mathbf{K}_T^{-1}\,\mathbf{f}\right) = \Delta\lambda_0\,\boldsymbol{\alpha}_T \tag{122}$$

where $\boldsymbol{\alpha}_T$ is the so-called tangential solution.

Equation (122) does not in general fulfill the equilibrium condition, i.e.

$$\boldsymbol{\Psi}\left(\boldsymbol{\alpha}_o + \Delta\boldsymbol{\alpha}\right) \neq \mathbf{0} \tag{123}$$

An iterative strategy is hence needed to find the new equilibrium point. For this purpose, it is convenient to split the displacement, $\boldsymbol{\alpha}_N$, and load, $\mathbf{f}_N$, vectors into three contributions: their previously converged values, $\boldsymbol{\alpha}_o$ and $\mathbf{f}_o$, the first incremental contributions, $\Delta\boldsymbol{\alpha}$ and $\Delta\mathbf{f}$, and the sum of the equilibrium iteration contributions, $d\boldsymbol{\alpha}_i$ and $d\mathbf{f}_i$, as follows

$$\boldsymbol{\alpha}_N = \boldsymbol{\alpha}_o + \Delta\boldsymbol{\alpha} + \sum_{i=1}^{N} d\boldsymbol{\alpha}_i \tag{124}$$

$$\mathbf{f}_N = \mathbf{f}_o + \Delta\mathbf{f} + \sum_{i=1}^{N} d\mathbf{f}_i \tag{125}$$

As previously mentioned, in order to overcome load limit points, we need to allow the load to vary during the equilibrium iterations. This can be achieved by modifying the definition of the out-of-balance force vector to include a load multiplication factor λ [20], i.e.

$$\boldsymbol{\Psi}\left(\boldsymbol{\alpha},\lambda\right) = \mathbf{K}_E\,\boldsymbol{\alpha} - \lambda\mathbf{f} \tag{126}$$

We derive now the "i+1th" contribution to the new equilibrium configuration. The Taylor expansion of the out-of-balance force vector as defined in (117) around the i^{th} iteration results $\left(\boldsymbol{\alpha}_i,\lambda_i\right)$ provides

$$\begin{aligned}\boldsymbol{\Psi}\left(\boldsymbol{\alpha},\lambda\right) &\cong \boldsymbol{\Psi}\left(\boldsymbol{\alpha}_i,\lambda_i\right) + \frac{\boldsymbol{\Psi}\left(\boldsymbol{\alpha}_i,\lambda_i\right)}{\partial\boldsymbol{\alpha}}\,d\boldsymbol{\alpha} + \frac{\boldsymbol{\Psi}\left(\boldsymbol{\alpha}_i,\lambda_i\right)}{\partial\lambda}\,d\lambda \\ &= \boldsymbol{\Psi}\left(\boldsymbol{\alpha}_i,\lambda_i\right) + \mathbf{K}_T\,d\boldsymbol{\alpha} - d\lambda\mathbf{f} = \mathbf{0}\end{aligned} \tag{127}$$

where $\boldsymbol{\Psi}\left(\boldsymbol{\alpha}_i,\lambda_i\right)$ is the out-of-balance force vector obtained in the previous iteration step. Hence, solving (127) we get

$$d\boldsymbol{\alpha} = d\boldsymbol{\alpha}_{i+1} = -\mathbf{K}_T^{-1}\,\boldsymbol{\Psi}\left(\boldsymbol{\alpha}_i, \lambda_i\right) + \mathbf{K}_T^{-1}\,d\lambda\mathbf{f} = d\boldsymbol{\alpha}_{i+1}^R + d\lambda_{i+1}\Delta\boldsymbol{\alpha} \tag{128}$$

where $d\boldsymbol{\alpha}_{i+1}$ is the i+1th contribution to the new equilibrium solution, $d\boldsymbol{\alpha}_{i+1}^R$ the increment in the solution deriving from the out-of-balance force, $\Delta\boldsymbol{\alpha}$ the tangential solution and the scalar function $d\lambda_{i+1}$ is the load modification factor which has to be specified according to an appropriate constraint.

Iteration strategy –The cylindrical arc-length method

The main difference between the available displacement methods is related to the constraint imposed on the load modification factor, $d\lambda_{i+1}$. As previously mentioned, the earliest methods iterated at constant load level, resulting in

$$d\lambda_{i+1} = 0 \tag{129}$$

A pure displacement control approach [19] starts with choosing the key control displacement parameter. The value of that parameter is incremented in the first step and then kept constant in the following equilibrium iterations. Denoting for example the key component as the n^{th} displacement, α_n, then

$$\alpha_n = \mathbf{b}_n^T\,\boldsymbol{\alpha} \tag{130}$$

in which $\mathbf{b}_n$ is a vector having zero entries except for unity in the n^{th} row. Imposing now the constraint during equilibrium iterations in (128)

$$d\alpha_n = \mathbf{b}_n^T\,d\boldsymbol{\alpha} = \mathbf{b}_n^T\,d\boldsymbol{\alpha}_{i+1}^R + d\lambda_{i+1}\left(\mathbf{b}_n^T\,\Delta\boldsymbol{\alpha}\right) = 0 \tag{131}$$

which provides the desired definition for the load modification factor, $d\lambda_{i+1}$ as

$$d\lambda_{i+1} = -\frac{\mathbf{b}_n^T\,d\boldsymbol{\alpha}_{i+1}^R}{\mathbf{b}_n^T\,\Delta\boldsymbol{\alpha}} \tag{132}$$

Other possible constraints have been proposed such as iterating the equilibrium equations at constant external work [19], minimizing the norm of incremental displacements, $\left\|d\boldsymbol{\alpha}\right\|$ [21], or the norm of the out-of-balance force vector $\left\|\boldsymbol{\Psi}\right\|$ [22]. The method which proved to be the most reliable and flexible is the so called arc-length method [23], which iterates along a hyper-spherical surface of constant radius l centred at the last converged state. To simplify the notation, it is convenient to introduce the definition

$$\Delta\boldsymbol{\alpha}_i^a = \Delta\boldsymbol{\alpha} + \sum_{k=1}^{i} d\boldsymbol{\alpha}_k \tag{133}$$

where $\Delta\boldsymbol{\alpha}_i^a$ is the incremental displacement accumulated at the i^{th} iteration step.

At the first incremental step, i.e. $i = 0$ the radius l of the hyper-sphere is expressed by

$$l^2 = \Delta\boldsymbol{\alpha}_0^{aT}\ \Delta\boldsymbol{\alpha}_0^a + \varphi^2 \Delta\lambda_0^2 \mathbf{f}^T\ \mathbf{f} \tag{134}$$

where the scalar parameter φ is unity in the original spherical arc-length method proposed independently by Riks [24] and Wempner [25], while it is zero in the cylindrical arc-length method subsequently proposed by Crisfield [26]. Due to its numerical stability, the latter has been used in the present work. At the i+1th equilibrium iteration the cylindrical arc-length is given by

$$l^2 = \Delta\boldsymbol{\alpha}_{i+1}^{a\ T}\ \Delta\boldsymbol{\alpha}_{i+1}^a \tag{135}$$

The accumulated incremental displacement is split into load and displacement related components as follows

$$\Delta\boldsymbol{\alpha}_{i+1}^a = \Delta\boldsymbol{\alpha}_i^a + d\boldsymbol{\alpha}_{i+1}^R + d\lambda_{i+1}\Delta\boldsymbol{\alpha} \tag{136}$$

The constant arc-length constraint then becomes

$$\left[\Delta\boldsymbol{\alpha}_i^a + d\boldsymbol{\alpha}_{i+1}^R + d\lambda_{i+1}\Delta\boldsymbol{\alpha}\right]^{T} \left[\Delta\boldsymbol{\alpha}_i^a + d\boldsymbol{\alpha}_{i+1}^R + d\lambda_{i+1}\Delta\boldsymbol{\alpha}\right] - l^2 = 0 \tag{137}$$

which leads to the quadratic expression in $d\lambda_{i+1}$

$$a\ \left(d\lambda_{i+1}\right)^2 + b\ d\lambda_{i+1} + c = 0 \tag{138}$$

where

$$a = \Delta\boldsymbol{\alpha}^T\ \Delta\boldsymbol{\alpha} \tag{139}$$

$$b = 2\left[\Delta\boldsymbol{\alpha}_i^a + d\boldsymbol{\alpha}_{i+1}^R\right]^{T}\ \Delta\boldsymbol{\alpha} \tag{140}$$

$$c = \left[\Delta\boldsymbol{\alpha}_i^a + d\boldsymbol{\alpha}_{i+1}^R\right]^{T} \left[\Delta\boldsymbol{\alpha}_i^a + d\boldsymbol{\alpha}_{i+1}^R\right] - l^2 \tag{141}$$

The solution of the quadratic expression in (138) leads to two possible roots, $d\lambda_{i+1}^1$ and $d\lambda_{i+1}^2$. One moves back along the equilibrium path and should

be discarded. The correct root is identified by, for each root, checking the angle, θ, between the new accumulated incremental displacement vector, $\Delta\boldsymbol{\alpha}_{i+1}^{a}$, and the accumulated incremental displacement vector obtained at the previous iteration, $\Delta\boldsymbol{\alpha}_{i}^{a}$. The angles are proportional to the scalar product of the two vectors,

$$\theta_{1,2} = \left[\Delta\boldsymbol{\alpha}_{i}^{a} + d\lambda_{i+1}^{1,2}\Delta\boldsymbol{\alpha} + d\boldsymbol{\alpha}_{i+1}^{R} \right]^{T} \Delta\boldsymbol{\alpha}_{i}^{a} \tag{142}$$

The correct root is the one providing a positive angle θ_i. If both angles are positive then the one closer to the linear root

$$d\lambda_{i+1}^{L} = -\frac{c}{b} \tag{143}$$

is chosen. If the determinant of (138) is negative, i.e. $b^2 - 4ac < 0$, then the initial load increment, $\Delta\lambda_0$, is probably too large and the structure exhibits more than one stability path at that point [27]. Ensuring a correct choice for the sign and magnitude of the initial load increment is of great importance for the convergence and efficiency of the method. This is discussed in detail in the following section.

Automatic load incrementation

Once a converged point on the equilibrium path is determined, the search for the next point starts by applying an initial load increment. In (121), the initial increment is defined by means of the scalar parameter $\Delta\lambda_0$ which defines the amount of the global external load vector, $\mathbf{f}$, to be initially applied. Both sign and magnitude of the initial increment strongly influence the convergence and efficiency of the numerical method and should reflect the degree of nonlinearity that the structure presents at that specific point [23]. The choice of too large values may slow the convergence or even trigger numerical difficulties, as mentioned in the previous section, while selecting a too small value leads to unnecessary computational effort because more equilibrium points than those strictly needed would be determined. Furthermore, once a load limit point is passed the applied load should decrease and not increase in the following step. It is then important to define a proper indicator for establishing the initial load increment sign.

The prediction of the magnitude of the initial load increment for a new equilibrium point is generally based on several parameters, including the initial load increment applied in the previous incremental step, $\Delta\lambda_0^o$, the number of iterations performed in the previous step to achieve convergence, J^o, and the

desired number of iterations at each step, J^d. The latter number of iterations, J^o, is an indicator of the local degree of nonlinearity of the global equilibrium path. An efficient automatic load increment strategy aims to make the number of equilibrium iterations as constant as possible for all equilibrium steps and close to the desired number, J^d. The closer to linear the equilibrium path, the smaller the number of iterations required to achieve equilibrium and hence the larger the desired initial increment. Conversely, in highly nonlinear segments of the equilibrium path, a small initial increment is required to keep the number of equilibrium iterations within an acceptable value.

The control key proposed by Crisfield [26] and Ramm [28] is the ratio

$$\left(\frac{J^d}{J^o} \right) \tag{144}$$

The general expression for the new automatic load increment is given by

$$\Delta\lambda_0^n = \pm\Delta\lambda_0^o \left(\frac{J^d}{J^o} \right)^\gamma \tag{145}$$

where the coefficient γ assumes values in the range from 0.5 to 1.0, and where assuming a smaller value produces more finely spaced equilibrium points. Equation (145) is directly applicable to load controlled methods, while for displacement controlled and generalized displacement controlled methods, the modified quantities are the key displacement and the arc-length respectively. The latter is of interest for the present work, and hence (145) is replaced by

$$l^n = l^o \left(\frac{J^d}{J^o} \right)^\gamma \tag{146}$$

The new initial load increment is hence derived by the definition of the arc-length given in (134) with $\varphi = 0$

$$\left(l^n \right)^2 = \Delta\boldsymbol{\alpha}_0^{aT}\ \Delta\boldsymbol{\alpha}_0^a = \Delta\boldsymbol{\alpha}^T\ \Delta\boldsymbol{\alpha} = \left(\Delta\lambda_0^n \right)^2 \boldsymbol{\alpha}_T^T\ \boldsymbol{\alpha}_T \tag{147}$$

and the new initial load increment is related to the new arc-length by

$$\Delta\lambda_0^n = \frac{\pm l^n}{\sqrt{\boldsymbol{\alpha}_T^T\ \boldsymbol{\alpha}_T}} \tag{148}$$

where l^n is given by (146).

After convergence to an equilibrium point, it is then possible to modify the arc-length and load increment for the next step using (146) and (148). For the first iteration, a starting value for the arc-length and the starting load increment need to be defined. This is generally achieved by setting the starting load increment to a value in the range of 20 to 40 percent of the anticipated maximum load [23]. The starting value of the arc-length is then calculated according to (147).

As mentioned previously, it is critical to choose the correct sign in (148). The wrong sign would lead the solution to double back along the equilibrium path rather than tracing new equilibrium points. The choice of whether the new initial load increment is to have the same sign as the previous or to reverse, is made by monitoring "test functions" which change sign when singular points are passed. Possible "test functions" are:

a) Determinant of the tangent stiffness matrix, $\det\left(\mathbf{K}_T\right)$;
b) Minimum pivot of the factorized tangent stiffness matrix, $D_{\min}$;
c) Current stiffness parameter, C_s;
d) Minimum eigenvalue of the tangent stiffness matrix, $\lambda_{\min}$.

Most numerical solution techniques compute the Crout factorization of the tangent stiffness matrix, i.e.

$$\mathbf{K}_T = \mathbf{L}\,\mathbf{D}\,\mathbf{L}^T \tag{149}$$

where $\mathbf{L}$ is a lower triangular unity matrix and $\mathbf{D}$ a diagonal matrix. The first two possible test functions can then be easily derived from (149), i.e.

$$\det\left(\mathbf{K}_T\right) = \prod_i D_{ii} \tag{150}$$

$$D_{\min} = \min\left(D_{ii}\right) \tag{151}$$

The so-called current stiffness parameter is related to the incremental external work performed by passing from the second last equilibrium configuration $\left(\boldsymbol{\alpha}^o, \mathbf{f}^o\right)$ to the last equilibrium point $\left(\boldsymbol{\alpha}^n, \mathbf{f}^n\right)$. Introducing the quantities

$$\Delta\boldsymbol{\alpha}^{n-o} = \boldsymbol{\alpha}^n - \boldsymbol{\alpha}^o \tag{152}$$

$$\Delta\mathbf{f}^{n-o} = \mathbf{f}^n - \mathbf{f}^o \tag{153}$$

we may define a scalar measure of the stiffness of the system, k, as "$k = \Delta\mathbf{f}^{n-o} / \Delta\boldsymbol{\alpha}^{n-o}$". With $\Delta\mathbf{f}^{n-o}$ and $\Delta\boldsymbol{\alpha}^{n-o}$ being vectors, the actual definition of the stiffness parameter k is obtained by multiplying the numerator and denominator by $\Delta\boldsymbol{\alpha}^{n-o}$, thus producing external works, i.e.

$$k = \frac{\left(\Delta \mathbf{f}^{n-o}\right)^T \Delta \boldsymbol{\alpha}^{n-o}}{\left(\Delta \boldsymbol{\alpha}^{n-o}\right)^T \Delta \boldsymbol{\alpha}^{n-o}} \tag{154}$$

The current stiffness parameter C_s is obtained by dividing k by its value at the very first load increment, k_0

$$C_s = \frac{k}{k_0} \tag{155}$$

Of the four possible choices, the one in d), $\lambda_{\min}$, is the most effective. Unfortunately, its calculation necessarily requires a computationally expensive eigenvalue analysis. Conversely, option a), $\det\left(\mathbf{K}_T\right)$, can be easily computed. For positive definite stiffness matrices all entries of the diagonal matrix **D** are strictly positive while once a load limit point is passed, one of the pivotal elements changes sign, implying a negative eigenvalue. Unfortunately a negative pivot may also be found once a bifurcation point is passed. Moreover, the determination of the sign based on option a) fails if an even number of pivotal negative entries is encountered. In these cases, the algorithm will generate a series of solutions oscillating around the singular point. The unstable equilibrium path past a bifurcation point can be followed using the test function in option c), C_s. Its sign reverses when passing a load limit point, while it remains unchanged if a bifurcation point is passed. Unfortunately, the current stiffness parameter reverses sign also after passing a displacement limit point. It follows that a consistent automatic load increment strategy cannot be based on one test function only. In the present work, both the determinant and the current stiffness parameter are monitored and the sign of the initial load increment switches only if both test functions reverse sign, excluding in this way both problems concerning bifurcation points and displacement limit points.

Convergence criteria

A force convergence criterion based on the out-of-balance vector, $\boldsymbol{\Psi}$, does not prove reliable for thin-walled structures. Once local buckling develops, it is difficult to decide whether moments or out-of-plane forces converge to an acceptable extent if there is no out-of-plane external loading on the structure [29]. For this reason, a displacement convergence criterion is here presented and adopted. The check is performed on the change in the incremental displacement field generated in the last i^{th} equilibrium iteration, $d\boldsymbol{\alpha}_i$

$$d\boldsymbol{\alpha}_i = d\boldsymbol{\alpha}_i^R \tag{156}$$

Bergan and Clough [30] suggest three different norms based on a scaled version of (156) for convergence checking. Dropping the subscript "*i*", we define:

The modified absolute norm

$$\left\|\varepsilon\right\|_1 = \frac{1}{N}\sum_{k=1}^{N}\left|\frac{d\alpha_k}{\alpha_{k,ref}}\right| \tag{157}$$

The modified Euclidean norm

$$\left\|\varepsilon\right\|_2 = \sqrt{\frac{1}{N}\sum_{k=1}^{N}\left(\frac{\delta\alpha_k}{\alpha_{k,ref}}\right)^2} \tag{158}$$

The maximum norm

$$\left\|\varepsilon\right\|_\infty = \max_k\left|\frac{\delta\alpha_k}{\alpha_{k,ref}}\right| \tag{159}$$

In (157), (158) and (159), N is the total number of degrees of freedom of the problem, $d\alpha_k$ is the k^{th} component of the last change in the incremental solution as defined in (156) and $\alpha_{k,ref}$ is the reference displacement of the same kind, e.g. increments in rotations are scaled on reference rotations. For the present work, the most stringent of the three possible norms defined above, the maximum norm, has been adopted. The equilibrium condition is considered fulfilled if

$$\left\|\varepsilon\right\|_\infty < \zeta_c \tag{160}$$

where ζ_c is the specified tolerance typically chosen in the range from 10^{-2} to 10^{-5} depending on the desired precision and on the nonlinearity of the problem.

Summary of the nonlinear solution strategy

A summary of the coded nonlinear procedures is given in the following. We assume that an equilibrium point, $(\boldsymbol{\alpha}_o, \mathbf{f}_o)$, has been found, and are looking for the new equilibrium point, $(\boldsymbol{\alpha}_n, \mathbf{f}_n)$. The reference external load vector is given as $\mathbf{f}$. The following steps are executed:

1. Evaluation of the stiffness parameter k from the last load and displacement increment according to (154)
$$\left(\Delta\boldsymbol{\alpha}^{n-o}, \Delta\mathbf{f}^{n-o}\right) \Rightarrow k;$$

2. Evaluation of the tangent stiffness matrix, $\mathbf{K}_T$ at the $\boldsymbol{\alpha}_o$ equilibrium configuration
$$\left(\boldsymbol{\alpha}_o\right) \Rightarrow \mathbf{K}_T;$$

3. Crout factorization of $\mathbf{K}_T$
$$\Rightarrow \det\left(\mathbf{K}_T\right);$$

4. Back-substitution to retrieve the tangential displacement vector $\Delta\boldsymbol{\alpha} = \mathbf{K}_T^{-1}\,\mathbf{f}$
$$\Rightarrow \Delta\boldsymbol{\alpha};$$

5. Automatic load increment, $\Delta\lambda_0^n$, calculation according to (146) and (148)
$$\left(l^o, \Delta\boldsymbol{\alpha}\right) \Rightarrow \pm\Delta\lambda_0^n;$$

6. Choice of the sign for the initial load increment depending on whether both the determinant of the stiffness matrix and the stiffness coefficient k changed sign in the last step on the equilibrium path
$$\left(\det\left(\mathbf{K}_T\right), k\right) \Rightarrow sign\left(\Delta\lambda_0^n\right);$$

7. The initial approximation is established as
$$\boldsymbol{\alpha}_o^1 = \boldsymbol{\alpha}_o + \Delta\lambda_0^n\Delta\boldsymbol{\alpha}$$
$$\lambda_o^1 = \lambda_o + \Delta\lambda_0^n$$
$$\mathbf{f}_o^1 = \mathbf{f}_o + \lambda_0^1\mathbf{f}$$

The initial step of the procedure is now concluded and the equilibrium iterations start. For $i \geq 1$

8. Evaluation of the out-of-balance vector, $\boldsymbol{\Psi}$, at $\left(\boldsymbol{\alpha}_o^i, \mathbf{f}_o^i\right)$ according to (100) and (101)
$$\left(\boldsymbol{\alpha}_o^i, \mathbf{f}_o^i\right) \Rightarrow \boldsymbol{\Psi};$$

9. Back-substitution to retrieve the residual displacement vector $d\boldsymbol{\alpha}_i^R = -\mathbf{K}_T^{-1}\,\boldsymbol{\Psi}$
$$\Rightarrow d\boldsymbol{\alpha}_i^R;$$

10. Convergence check according to (159)

$$\left(\boldsymbol{\alpha}_o^i, d\boldsymbol{\alpha}_i^R\right) \Rightarrow \begin{cases} \text{convergence} \Rightarrow \text{ go to 13.} \\ \text{not convergence} \Rightarrow \text{ go to 11.} \end{cases}$$

11. Arc-length method implementation:
    - determination of the constants *a*, *b* and *c* according to (139), (140) and (141)
    $$\left(\boldsymbol{\alpha}_o^i, d\boldsymbol{\alpha}_i^R\right) \Rightarrow a, b, c;$$
    - determination of the "angles" θ_1 and θ_2 according to (142);
    - choice of the proper root for (138) providing the load increment correction, $d\lambda_i$
    $$\left(\theta_1, \theta_2\right) \Rightarrow d\lambda_i;$$

12. The new approximation is established as

$$\boldsymbol{\alpha}_o^{i+1} = \boldsymbol{\alpha}_o^i + d\lambda_i\, \Delta\boldsymbol{\alpha} + d\boldsymbol{\alpha}_i^R$$
$$\lambda_o^{i+1} = \lambda_o^i + d\lambda_i$$
$$\mathbf{f}_o^{i+1} = \mathbf{f}_o^i + d\lambda_i \mathbf{f};$$

Steps 8 to 12 are repeated until the convergence check in 10 is satisfied.

13. Once the new equilibrium point has been found the solution is updated as

$$\boldsymbol{\alpha}_n = \boldsymbol{\alpha}_o^i$$
$$\lambda_n = \lambda_o^i$$
$$\mathbf{f}_n = \mathbf{f}_o^i$$

The procedure may now be repeated from point 1 to define the next point on the equilibrium path.

Increment cutting facility

Situations may arise when the numerical procedure fails due to a slow convergence rate or non-convergence. A slow convergence rate may be encountered in a modified Newton-Raphson procedure when entering highly nonlinear parts of the equilibrium path. For the arc-length method, these difficulties become evident in two possible ways: either the number of iterations required to achieve equilibrium exceeds a certain value, normally set in the range from 15 to 20, or the discriminator of the quadratic form in (138) is negative. In both cases, the procedure has to be interrupted and restarted from the last converged equilibrium point adopting a reduced initial load increment.

The new initial load increment should preferably be within the range from 10 to 50 percent of the last one adopted. In the present work the value of 50 percent has been chosen.

Initial imperfections

In solving nonlinear problems it is generally important to introduce initial imperfections triggering the nonlinear behaviour at an early loading stage. In the buckling of thin-walled structures in particular, the post-critical branch is usually influenced by local out-of-plane or distortional imperfections to which no corresponding external imposed load exists. Hence it is important to make an ad-hoc facility available which can generate or read an appropriate initial deformed shape. When actual imperfection measurements of the physical specimen are not available, the two most common ways of generating initial imperfections are to use a linear analysis of the structure subject to special load distributions or an elastic buckling analysis. The former is the more economical option from a numerical point of view but for a complex structure or a complex geometric imperfection it may be cumbersome to define a proper load distribution that provides the desired deformed shape. Conversely, an elastic buckling analysis is computationally more demanding and requires a more sophisticated numerical code, but automatically provides the desired buckled shape for the given structure subject to given loads. The present work takes advantage of the computer codes developed for the linear analysis and the elastic buckling analysis by the isoparametric spline finite strip method, and allows a pre-analysis of the structure according to either of the two methods to define the initial imperfections. The initial displacements are computed at the pre-analysis stage and utilized in all the following step of the nonlinear analysis.

Examples of elastic nonlinear analysis

In the first example, the ability of the incremental-iterative strategy here adopted to overcome singular points of any type is shown with application to an eccentrically loaded circular arch.

Classical examples of the post buckling behaviour of square plates are then presented where the results are compared to exact solutions and numerical solutions by other researchers.

Moreover, a series of examples of nonlinear analysis of perforated flat and stiffened plates is presented. The results obtained with the isoparametric spline finite strip analysis are compared with results obtained using the commercial finite element method software Abaqus.

Circular shallow arch subject to an eccentric concentrated force

In this example, a circular shallow arch is subjected to a concentrated eccentric load. This problem was solved by other authors including Harrison [31] and Clarke [23], and has been chosen for its complex geometrical nonlinear features. It presents snap-through and snap-back behaviour, four load limit points and two displacement limit points. Its geometry is shown in Fig. 5.

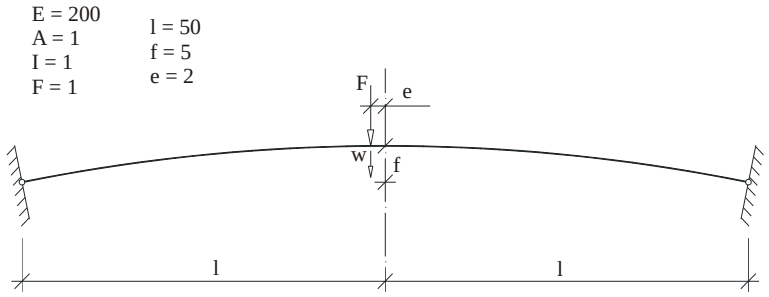

Fig. 5: Circular arch subject to eccentric concentrated load.

The arch has been modelled with 12 plane strips running in the out-of-plane direction while both Harrison and Clarke used isoparametric beam elements reproducing also the curvature of the arch. The simulation has been performed assuming a Poisson's ratio equal to zero.

The equilibrium path obtained is shown in Fig. 6. The agreement is very good in the maximum load limit points areas, while the results around the minimum load limit points differ slightly. The discrepancy could be anticipated, due to the different geometric models utilized. Nevertheless, the main nonlinear path of this particular structural problem has been predicted by the method proposed, proving its ability to overcome the traditional challenges of geometric nonlinear analysis.

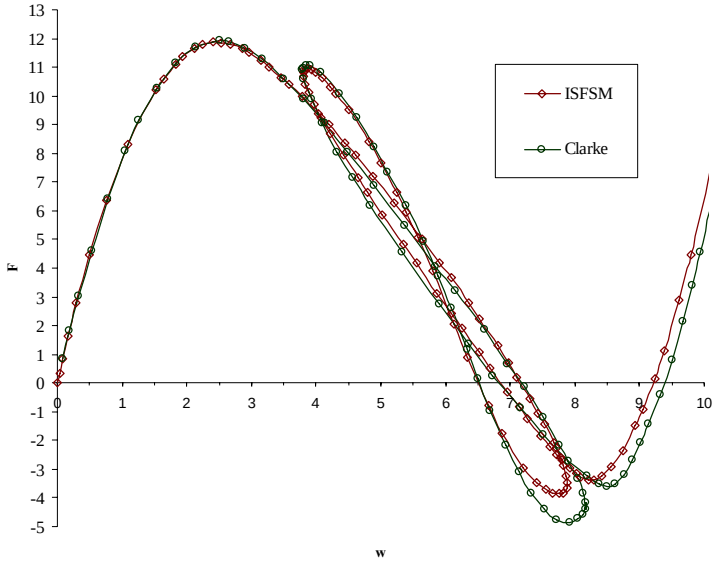

Fig. 6: Equilibrium path for an eccentrically loaded arch.

Cylindrical shallow shell subject to a concentrated force

Another numerically challenging problem consists of a cylindrical shell loaded by a concentrated load at midspan, as shown in Fig. 7. This example has been analysed by Oliver [32] and Kwon [29] and, presenting two load limit points, it has been chosen to prove the capability of the method to pass limit points for two-dimensional problems. As in Kwon [10], the shell has been discretised with plane strips and, due to its symmetry, only a quarter of the structures has been analysed.

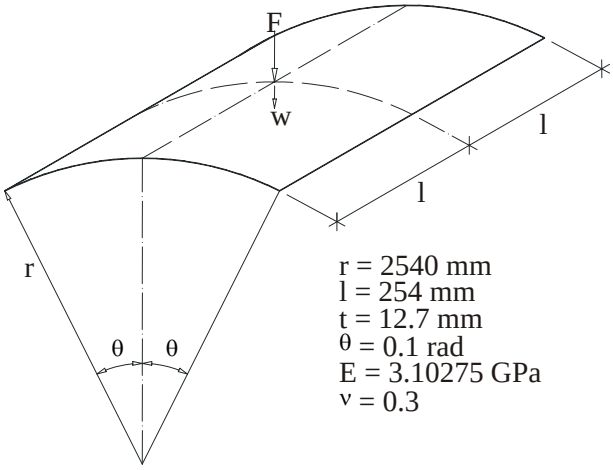

Fig. 7: Cylindrical shell subject to concentrate centred load.

The results are compared in Fig. 8 and a good agreement between the three different analyses can be observed.

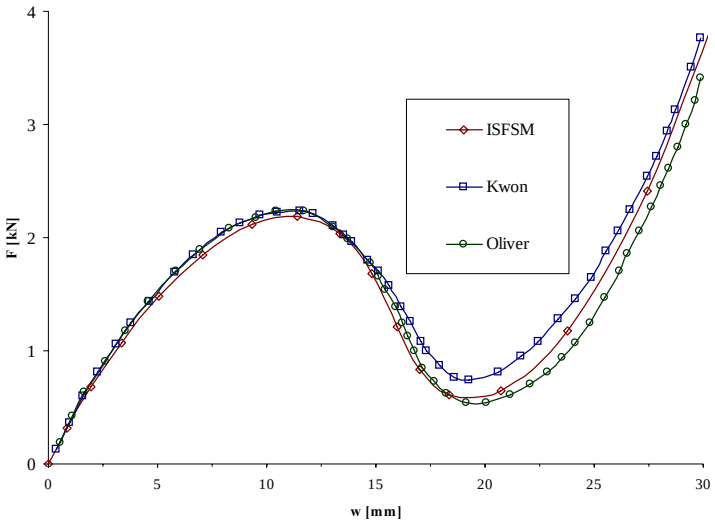

Fig. 8: Equilibrium path for a cylindrical shell centrally loaded.

In-plane buckling of a strut

The capability of the isoparametric spline finite strip method to analyse in-plane second order deformations is tested next. A strut completely restrained from out-of-plane displacements and simply supported for in-plane displacements is axially loaded as shown in Fig. 9. The nonlinear response is triggered by an initial imperfection, given by the buckled shape, as provided by a linear elastic buckling analysis and shown by the solid line in Fig. 9.

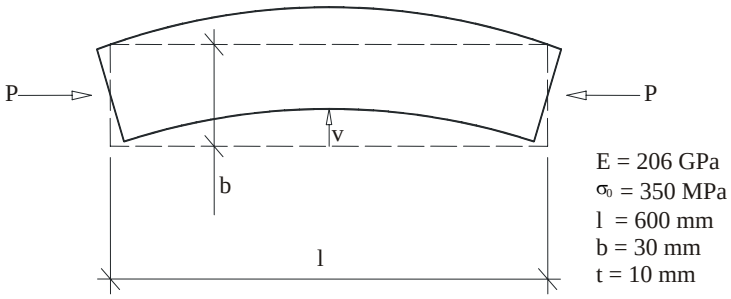

Fig. 9: In-plane Euler buckling of a strut.

Three different values for the maximum imperfection at midspan have been presented in this example, showing how at decreasing imperfections the response approaches the asymptotic value of the Euler buckling load, represented by the dashed line in Fig. 10. The results are compared with the curves obtained by Key [33] and by Kwon and Hancock [29]. Good agreement can be noticed.

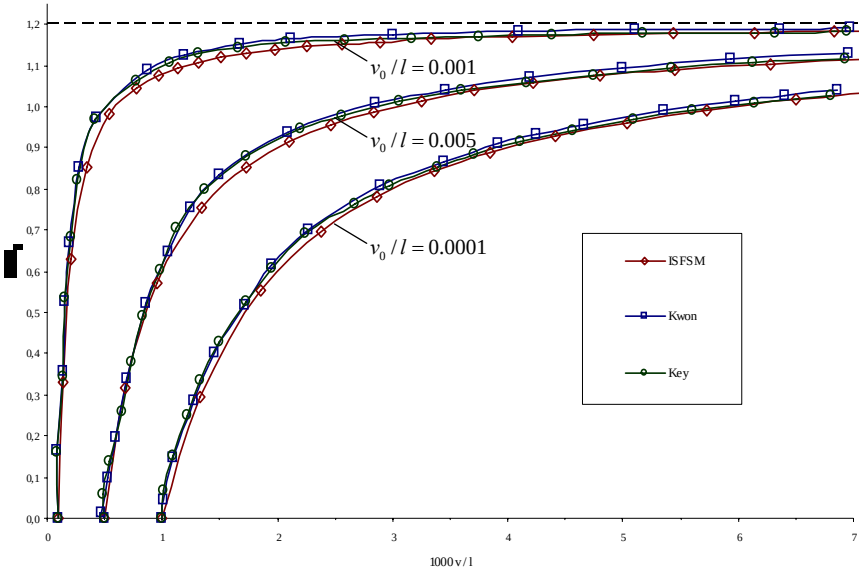

Fig. 10: Equilibrium path for a axially loaded strut.

Square plate in edge compression

A classical example of plate post-buckling resistance is presented. The plate is assumed to be square and simply supported in the out-of-plane direction along its perimeter. While its longitudinal edges are completely free to move in the in-plane directions, the transverse loaded edges are compressed by frictionless platens providing a uniform deformation. An initial out-of-plane imperfection in the shape of the critical elastic buckling mode is considered having its maximum value at the plate centre equal to ten percent of the plate thickness. The geometry of the problem is shown in Fig. 11. This particular problem has been analysed theoretically by Yamaki [34]. The numerical results obtained are hence compared to nearly exact ones.

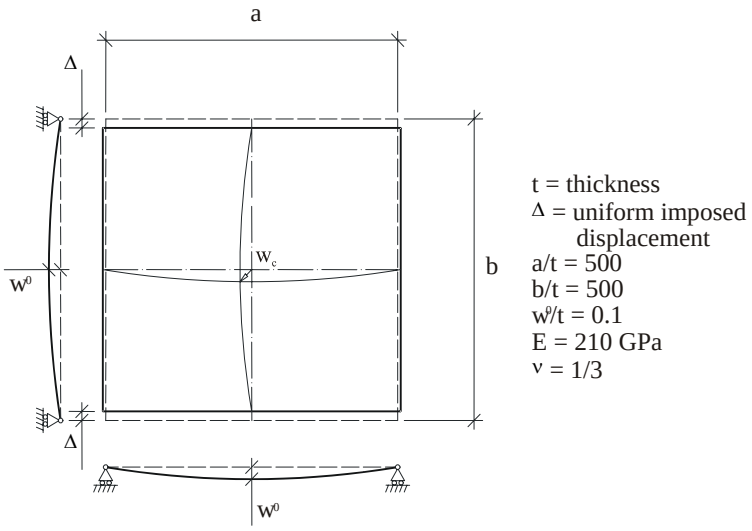

Fig. 11: Simply supported square plate subject to uniform shortening.

Fig. 12 illustrates the comparison where a perfect agreement is found in the post-critical branch while some minor differences are observed in the pre-critical path. In Fig. 12, the curve obtained by applying a uniform stress along the compressed edges is also shown to illustrate the typical softer post-buckling branch. The load factor λ is given by the ratio

$$\lambda = \frac{\overline{p}_y a^2}{\pi^2 E t^2} \tag{161}$$

where $\overline{p}_y$ is the average stress along the loaded edges, a their length and t the thickness of the plate.

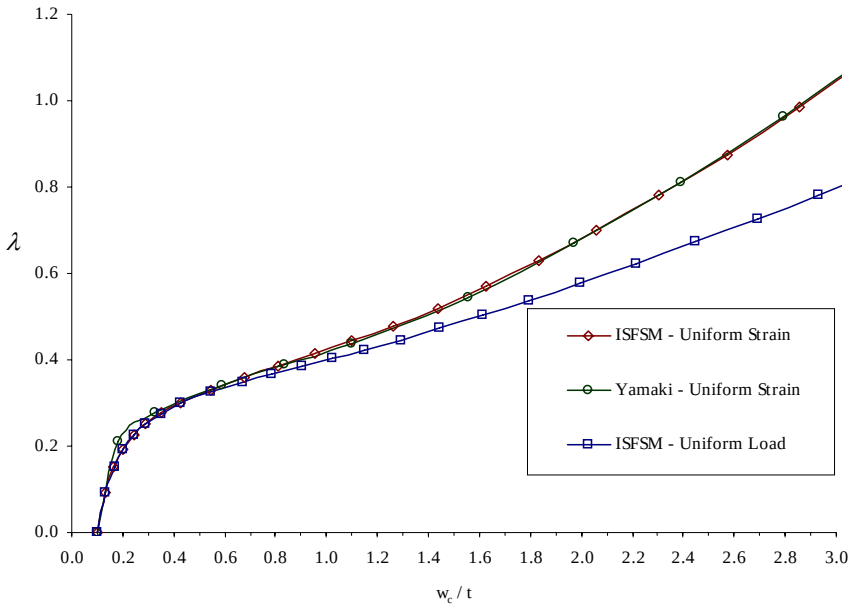

Fig. 12: Equilibrium path of a square plate in uniform mono-axial strain.

Channel section in axial compression

A stiffened thin-walled channel section in axial compression is analysed to investigate the capability of the method to solve distortional buckling problems. Other authors have previously considered this example, including Sridharan [35] and Key [33] who applied the semi-analytical finite strip method, and Kwon [29] who applied the spline finite strip method. In the analyses, a distortionally buckled cell was analysed, taken as a full distortional buckled wavelength, as obtained using an elastic buckling analysis. Fig. 13 illustrates the buckled cell shape. Symmetry in terms of in-plane rotations has been applied at the ends of the element, which are considered compressed by frictionless platens. The initial imperfection is obtained from an elastic buckling analysis and corresponds to the distortional buckled shape having an amplitude, $\delta_{e0} = \delta_{m0}$, of one percent of the thickness of the section. Sridharan and Key modelled the entire distortionally buckle cell, Fig. 13 (a), while Kwon exploited the symmetry of the problem and analysed only a half wave-length as shown in Fig. 13 (b). In the present work, the latter model has been utilized. In Fig. 14, the curves obtained by the different researches are compared. Plotting the equilibrium path for the displacement, δ_e, at the end section we note that the curve obtained by the present method closely follows the curve obtained by Kwon. The curve representing the equilibrium path for the midspan displacement, δ_m, follows closely the stiffer trend described by Key. The different behaviour is due to the coupling of distortional and local buckling which gradually localizes the distortion in the loaded areas at the end of the section, where the free edges of the lips develop compression, while the central

portion of the element tends to a distortional buckled shape without local deformations of the lips.

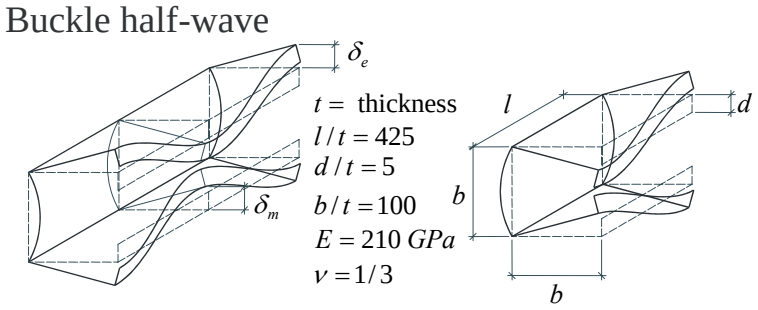

Fig. 13: Distortionally buckled channel section.

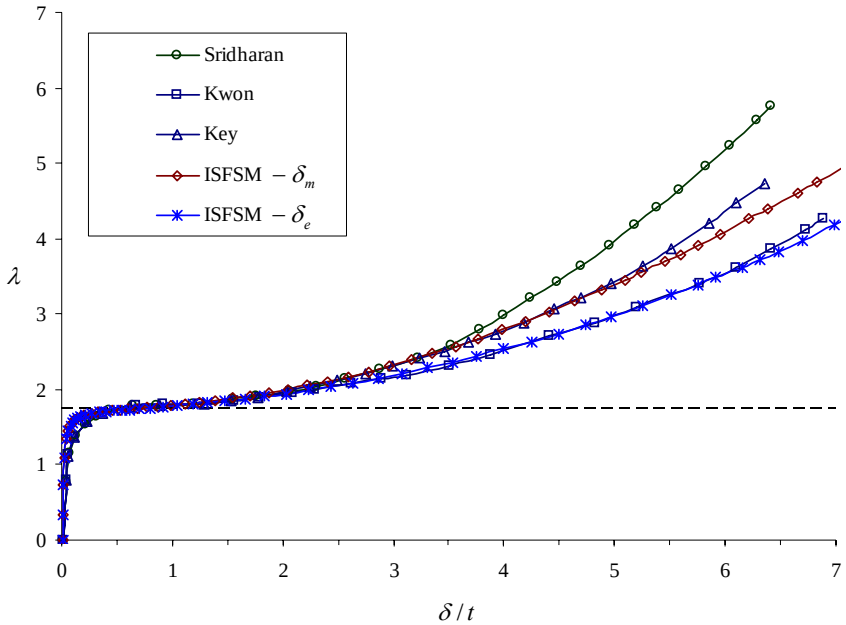

Fig. 14: Equilibrium paths of a distortionally buckled channel section.

Examples of elastic nonlinear analysis of perforated flat and stiffened plates

Two examples of geometrical nonlinear analysis of perforated thin-walled elements are given in the following. Both perforated flat plates and perforated stiffened plates are considered. The stiffened plate is a modification of the flat plate analysed, where a longitudinal web stiffener is introduced while keeping all other dimensions the same. The numerical examples highlight the enhanced performance obtained in stiffened plates with regard to buckling.

The results obtained with the isoparametric spline finite strip analysis are compared with the results obtained with the commercial finite element software Abaqus [36]. Comparisons are made of the overall load-shortening curve, the

out-of-plane displacement in selected reference points and Von Mises stresses on the outside and inside surfaces of the elements. In the finite element analysis, eight node quadratic shell elements have been utilised.

Geometric nonlinear analysis of a square flat plate with diamond perforations

The geometry of the plate analysed in this example is shown in Fig. 15. The plate is simply supported in the out-of-plane direction and the longitudinal edges are restrained in the transverse direction. The top transverse edge is loaded by an ideal frictionless platen applying a uniform axial shortening, as shown in Fig. 16 (a). The meshes used in the isoparametric spline finite strip and finite element analyses are shown in Fig. 16 (b) and Fig. 16 (c), respectively. The number of degrees of freedom and elements are compared in Table 1.

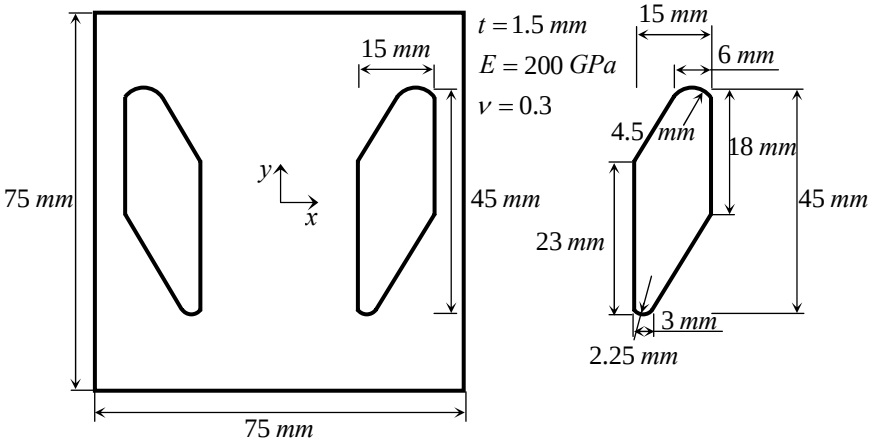

Fig. 15: Geometry of the square plate with diamond perforations.

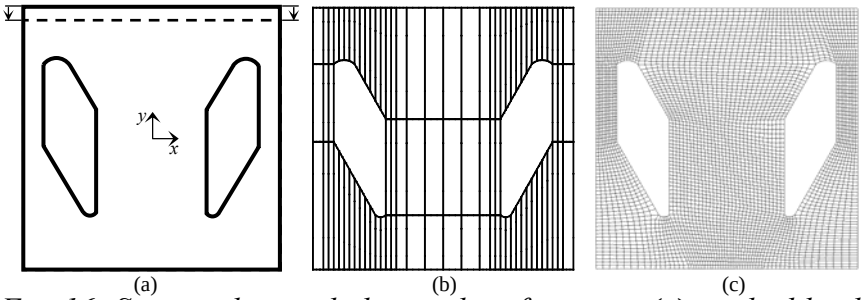

Fig. 16: Square plate with diamond perforations: (a) *applied load;* (b) *Isfsm mesh;* (c) *Fem mesh.*

	Strips (Elements)	Nodes	Dofs
ISFSM	88	5473	27365
FEM/ABAQUS	4253	13234	79404
Ratio FEM/ISFSM	48.3	2.4	2.9

Table 1: Diamond perforations, mesh comparison.

The initial imperfection is in the shape of the first buckling mode (Fig. 17 (a)), as obtained from and elastic buckling analysis performed according to [4]. The maximum initial deflection is equal to 0.15 *t*, where *t* is the uniform thickness of the plate, equal to 1.5 mm.

The geometrical nonlinear analysis is performed up to the limit of 2.5 times the critical shortening. The final deformed shape is shown in Fig. 17 (b).

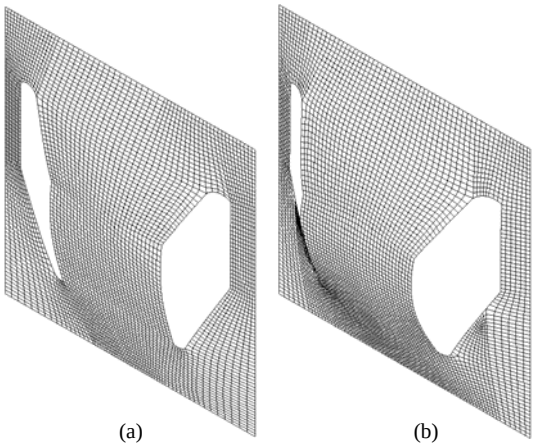

Fig. 17: Square plate with diamond perforations: (a) *initial imperfections; (b) final deformed shape.*

The load *vs* end shortening response of the plate is shown in Fig. 18. As in previous examples, buckling causes a reduction in the slope of the curves in the vicinity of the critical shortening of about 0.05 mm.

Buckling mainly occurs in the central part of the plate as shown by the deflection curves in Fig. 19, and the Von Mises stress curves in Fig. 20.

Overall, the agreement between the two numerical analyses is good. The maximum difference of about five percent is found for the Von Mises stress at point *C* which is in an area of high stress gradient. The isoparametric spline finite strip method produces higher stress values than the finite element method for given values of shortening. The difference is attributed to the stress smoothing technique utilised in Abaqus.

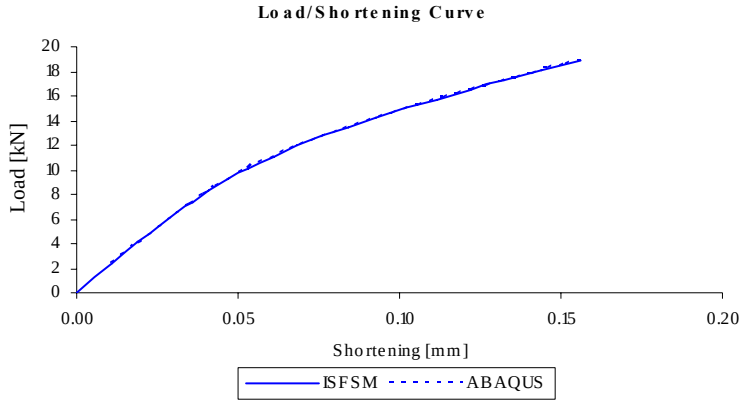

Fig. 18: Square plate with diamond perforations, load-shortening curve.

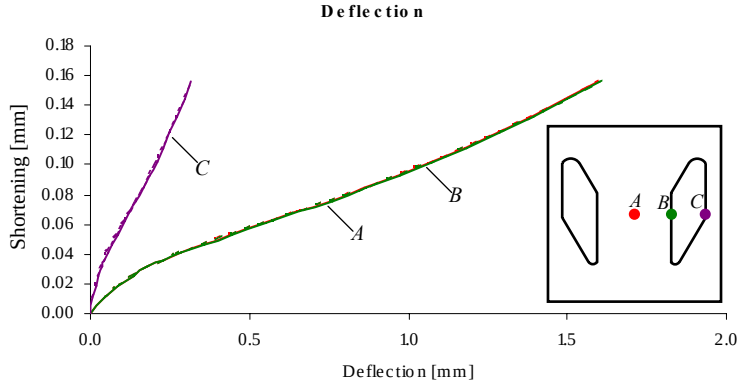

Fig. 19: Square plate with diamond perforations, deflections curves.

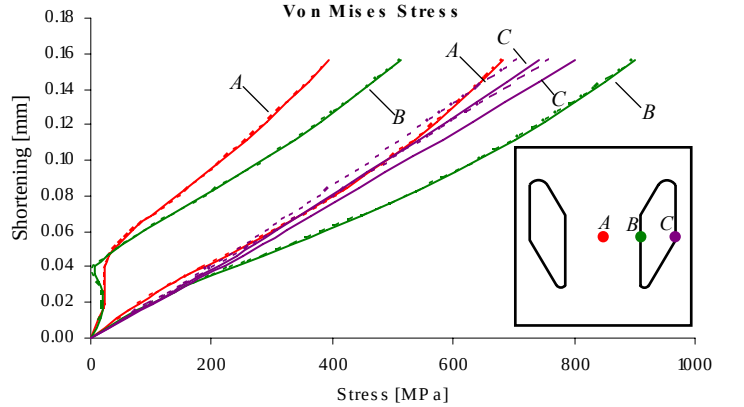

Fig. 20: Square plate with diamond perforations, Von Mises stress curves.

Geometric nonlinear analysis of a stiffened plate with diamond perforations

The geometry of the analysed stiffened plate is shown in Fig. 21. The support conditions are the same as those used for the flat plate with diamond-shaped perforations. A uniform axial shortening is applied to the top transverse edge, as shown in Fig. 22 (a). The plate is discretised according to the meshes shown in

Fig. 22 (b) and Fig. 22 (c). The number of degrees of freedom and elements are compared in Table 2.

The shape of the initial imperfection is shown in Fig. 23 (a) which corresponds to the second buckling mode obtained by an elastic buckling analysis. The geometrical nonlinear analysis is performed until the limit of 2.5 times the critical shortening. The final deformed shape obtained in the analysis is shown in Fig. 23 (b).

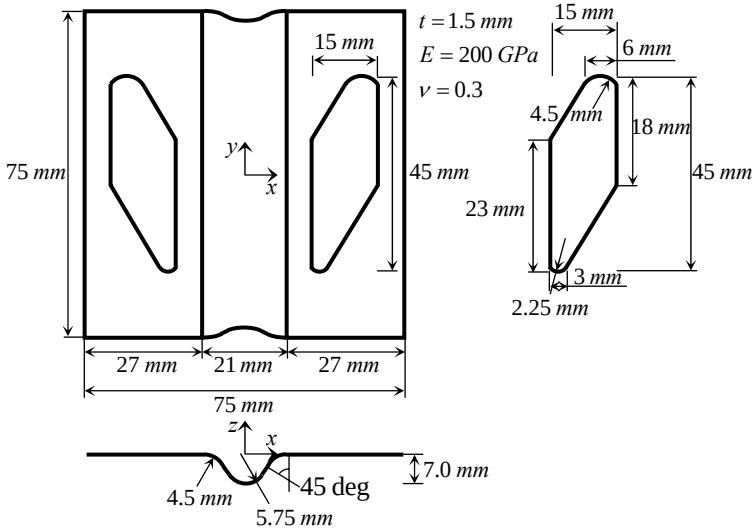

Fig. 21: Geometry of the stiffened plate with diamond perforations.

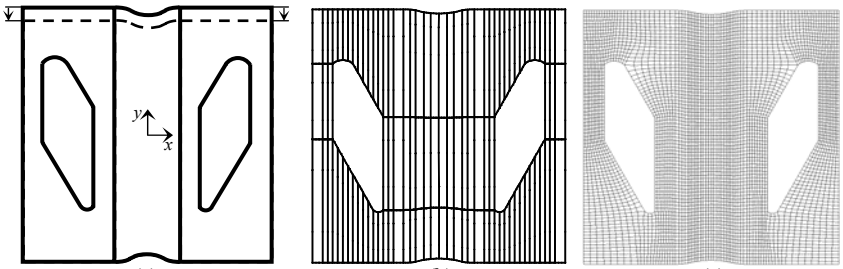

Fig. 22: Stiffened plate with diamond perforations: (a) *applied load;* (b) *Isfsm mesh;* (c) *Fem mesh.*

The overall load-shortening response of the plate is shown in Fig. 24. The softening effect due to buckling can be observed by comparing the initial and final slopes of the load-shortening curve.

The deflections at four reference points are shown in Fig. 25. The larger deflections of the central part of the element can be noted by comparing the curves for points *A* and *B* with those for points *C* and *D*. Furthermore, the Von Mises stresses at the four reference points are shown in Fig. 26 and in Fig. 27. Large bending stresses (difference between stresses at the two surfaces) can be observed at points *C* and *D* (the latter in the post-critical range), while minor bending stresses gradually develop at points *A* and *B*.

	Strips (Elements)	Nodes	Dofs
ISFSM	106	6463	32920
FEM/ABAQUS	5172	16017	96102
Ratio FEM/ISFSM	48.8	2.5	2.9

Table 2: Stiffened plate with diamond perforations, mesh comparison.

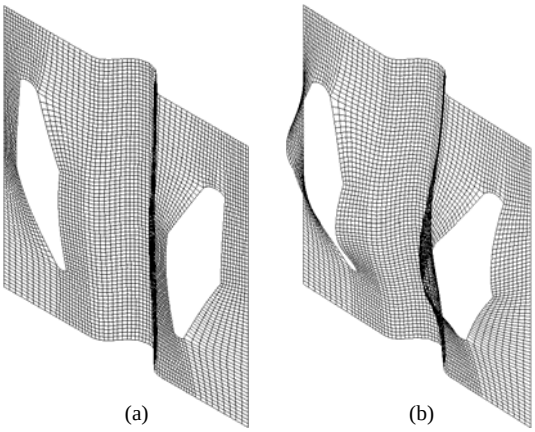

Fig. 23: Stiffened plate with diamond perforations: (a) *initial imperfections; (b) final deformed shape.*

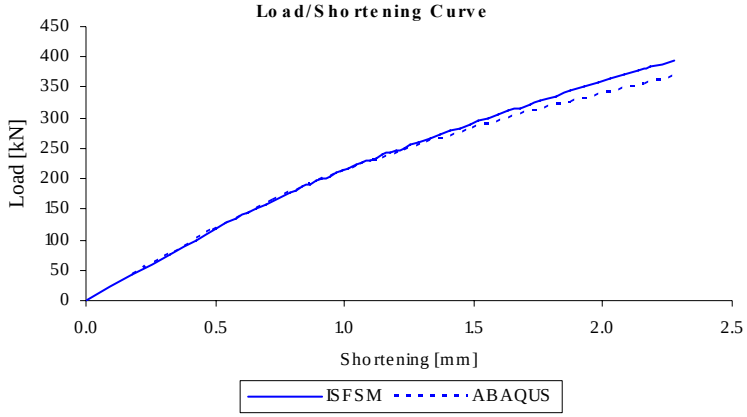

Fig. 24: Stiffened plate with diamond perforations, load-shortening curve.

A good agreement is observed between the isoparametric spline finite strip results and finite element results, both in terms of deflection and stress, at reference points *A*, *B* and *C*. The post-buckling behaviour predicted for point *D* differs between the two analyses. The isoparametric spline finite strip analysis describes a gradual buckling of the outer regions of the element, while a softer behaviour is encountered in the finite element analysis (dashed curves in the graphs). This difference can also be noted in the overall response of the element, Fig. 24, which shows a stiffer post-buckling behaviour in the curve related to the isoparametric spline finite strip analysis (maximum difference of about 7

percent in load at a shortening of 2.25 mm). The area around point *D* the deflection varies rapidly from zero, along the supported edge, to 4 mm at point *D* at a shortening of 2.25 mm (Fig. 25), consequently producing large rotations. The relations given in (43)-(45) only accounts for moderate rotations, hence, a possible explanation for the discrepancies in Fig. 24, Fig. 25 and Fig. 27

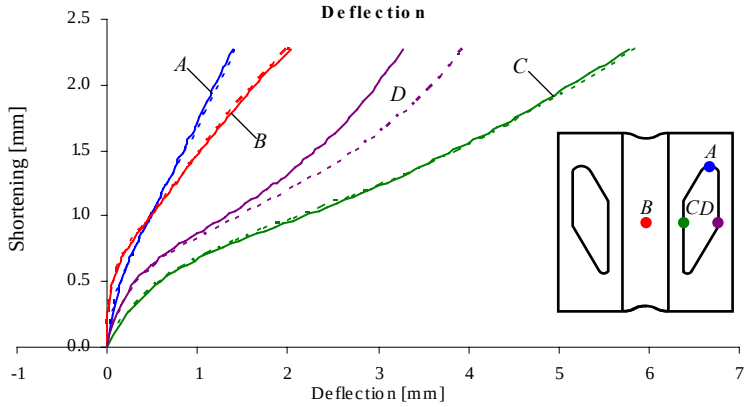

Fig. 25: Stiffened plate with diamond perforations, deflections curves.

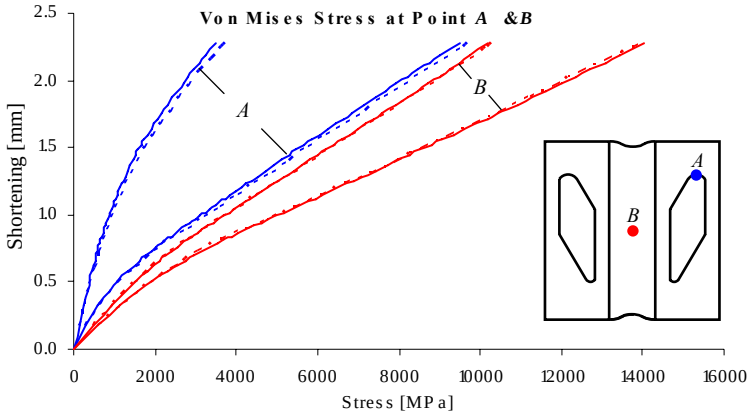

Fig. 26: Stiffened plate with diamond perforations, Von Mises stress curves at points A and B.

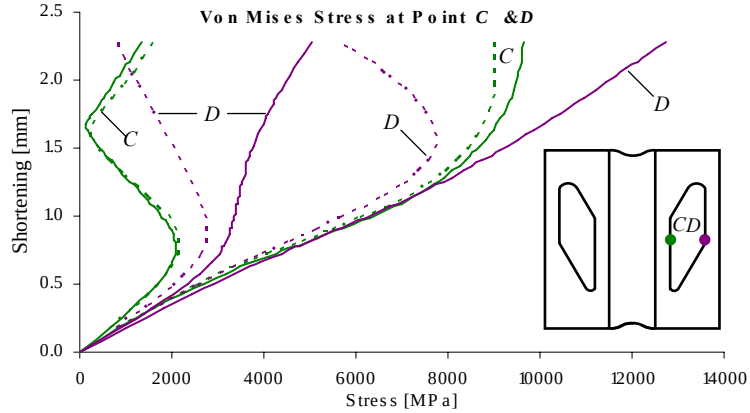

Fig. 27: Stiffened plate with diamond perforations, Von Mises stress curves at points C and D.

Conclusions

The geometric nonlinear analysis of thin-walled structures by the isoparametric spline finite strip method has been presented. The general elastic nonlinear theory has been discussed in detail by describing the kinematics assumption, the strain-displacements relations, the material constitutive relations and the equilibrium equations. The theory has been applied to derive a matrix formulation for the isoparametric spline finite strip method which can be readily coded in a computer program.

The available techniques for solving nonlinear problems have been presented, notably the cylindrical arc-length method. The principal steps of the procedure have been discussed and particular attention has been paid to defining the critical parameters that allow the procedure to follow complex structural nonlinear behaviours, such as snap-through and snap-back, as encountered at load and displacement limit points.

A number of examples has been presented to demonstrate the efficiency and reliability of the isoparametric spline finite strip method. The first series of examples dealt with the solution of challenging classical nonlinear problems for which reliable solutions are available in the literature. The second series of example applied the geometric nonlinear isoparametric spline finite strip analysis to perforated flat plates and perforated stiffened plates. The results obtained with the isoparametric spline finite strip method have been shown to generally agree closely with results obtained with commercial finite element software. Discrepancies were encountered in the vicinity of areas with large rotations where the isoparametric spline finite strip method predicted a stiffer response than the finite element method.

References

[1] Eccher, G, Rasmussen, KJR, Baldassino, N, Zandonini, R. Isoparametric Spline Finite Strip Method for In-plane Stress Analysis. The University of Sydney, Department of Civil Engineering, R848, 2005.

[2] Eccher, G, Rasmussen, KJR, Zandonini, R. Isoparametric spline finite strip method for the bending of perforated plates. School of Civil Engineering, The University of Sydney, Sydney, Australia, R877, 2007.

[3] Eccher, G, Rasmussen, KJR, Zandonini, R. Linear elastic isoparametric spline finite strip analysis of perforated thin-walled structures. School of Civil Engineering, The University of Sydney, Sydney, Australia, R878, 2007.

[4] Eccher, G, Rasmussen, KJR, Zandonini, R. Elastic buckling analysis of perforated thin-walled structures by the isoparametric spline finite strip method School of Civil Engineering, The University of Sydney, Sydney, Australia, R879, 2007.

[5] Cheung, YK. Finite strip method in structural analysis. Oxford ; New York: Pergamon Press, 1976.
[6] Cheung, YK, Fan, SC, Wu, CQ. Spline finite strip in structural analysis. In: editors. Proceedings of the Proceedings of the International Conference on Finite Element Method. Shanghai, China: 1982
[7] Fan, SC, Spline finite strip in structural analysis., Thesis, University of Hong Kong, 1982.
[8] Lau, SCW, Hancock, GJ. Inelastic buckling analysis of beams, columns and plates using the spline finite strip method. Thin-Walled Structures 1989; 7:213-238.
[9] Lau, SCW, Hancock, GJ. Buckling of thin flat-walled structures by a spline finite strip method. Thin-Walled Structures 1986; 4(4):269-294.
[10] Kwon, YB, Hancock, GJ. A nonlinear elastic spline finite strip analysis for thin-walled sections. Thin-Walled Structures 1991; 12(4):295-319.
[11] Au, FTK, Cheung, YK. Isoparametric spline finite strip for plane structures. Computers & Structures 1993; 48(1):23-32.
[12] Cheung, YK, Au, FTK. Isoparametric spline finite strip for degenerate shells. Thin-Walled Structures 1995; 21(1):65-92.
[13] Godley, MHR. Storage Racking - chapter 11. In: editors. Design of Cold Formed Steel Members. Ed. Rhodes, 1991.
[14] Shanmugam, NE, Thevendran, V, Tan, YH. Design formula for axially compressed perforated plates. Thin-Walled Structures 1999; 34(1):1.
[15] Shanmugam, NE, Thevendran, V. Lateral buckling of doubly symmetric beams containing openings. Journal of Engineering Mechanics, American Society of Civil Engineers 1991; 117(7):1427-1441.
[16] Shanmugam, NE, Dhanalakshmi, M. State of art review and compilation of studies on perforated thin-walled structures. International Journal of Structural Stability and Dynamics 2001; 1
[17] Rhodes, J, Macdonald, M. The effect of perforation length on the behaviour of perforated elements in compression. In: editors. Proceedings of the Thirthteenth International Speciality Conference on Cold-Formed Steel Structures. 1996
[18] Zienkiewicz, OC. The Finite Element Method. London: McGraw-Hill, 1977.
[19] Powell, G, Simons, J. Improved iteration strategy for nonlinear structures. International Journal for Numerical Methods in Engineering 1981; 17:1455-1467.
[20] Crisfield, MA. Non-linear finite element analysis of solids and structures. Volume 1. Wiley, 1991.
[21] Chan, SL. Geometric and material nonlinear analysis of beam-columns and frames using the minimum residual displacement method. International Journal for Numerical Methods in Engineering 1988; 26:2657-2669.
[22] Bergan, PG. Solution algorithms for nonlinear structural problems. Computers & Structures 1980; 12:497-509.

[23] Clarke, MJ, Hancock, GJ. A study of incremental-iterative strategies for non-linear analysis. International Journal for Numerical Methods in Engineering 1990; 29:1365-1391.
[24] Riks, E. An incremental approach to the solution of snapping and buckling problems. International Journal of Solids and Structures 1979; 15:529-551.
[25] Wempner, GA. Discrete approximations related to nonlinear theories of solids. International Journal of Solids and Structures 1971; 7:1581-1599.
[26] Crisfield, MA. A fast incremental/iterative solution procedure that handles "snap-through". Computers & Structures 1981; 13:55-62.
[27] Meek, JL, Tan, HS. Geometrically nonlinear analysis of space frames by an incremental iterative technique. Computer Methods in Applied Mechanics and Engineering 1984; 47:261-282.
[28] Ramm, E. Strategies for tracing the nonlinear response near limit points. In: Wunderlic, editors. Nonlinear Finite Element Analysis in Structural Mechanics. Berlin: Springler-Verlag, 1981.
[29] Kwon, YB, Hancock, GJ. A nonlinear elastic spline finite strip analysis for thin-walled sections. Thin-Walled Structures 1991; 12:295-319.
[30] Bergan, PG, Clough, RW. Convergence criteria for iterative processes. American Institute of Aeronautics and Astronautics Journal 1972; 10:1107-1108.
[31] Harrison, HB. Structural Analysis and Design: Some Microcomputer Methods. Oxford: Pergamon Press, 1980.
[32] Oliver, J, Onate, E. A total lagrangian formulation for the geometrcally nonlinear analysis of structures using finite elements; shell and plate structures. International Journal for Numerical Methods in Engineering 1984; 20:2253-2287.
[33] Key, PW, The behaviour of cold-formed square hollow section columns Thesis, Civil and Mining Engineering University of Sydney, 1988.
[34] Yamaki, N. Postbuckling behaviour of rectangular plates with small initial curvature loaded in edge compression. Journal of Applied Mechanics 1959; 81(E):407-414.
[35] Sridharan, S. A semi-analytical method for the posl-local-torsional buckling analysis of prismatic plate structures International Journal for Numerical Methods in Engineering 1982; 18:1685-1697.
[36] ABAQUS/STANDARD. User's Manual Version 6.5. Hibbit, USA: Karlsson & Sorensen, 2006.